Semi-analytical IGA-based computation of wave dispersion in fluid-coupled anisotropic poroelastic plates

Vu-Hieu Nguyen, Fakhraddin Seyfaddini, H. Nguyen-Xuan

Semi-analytical IGA-based computation of wave dispersion in fluid-coupled anisotropic poroelastic plates

Fakhraddin Seyfaddini[a], Hung Nguyen-Xuan[b], Vu-Hieu Nguyen[a]

[a] *MSME, CNRS UMR 8208, Univ Paris Est Creteil, Univ Gustave Eiffel, F-94010 Creteil, France.*
[b] *CIRTech Institute, Ho Chi Minh City University of Technology (HUTECH), 475 Dien Bien Phu, P2, Binh Thanh, Ho Chi Minh City, Vietnam*

Abstract

Understanding dispersion relations and wave mode shapes is vital in nondestructive control of dynamic behaviors of poroelastic composites. In the framework of semi-analytical finite element (SAFE) method, this paper presents two numerical approaches so-called semi-analytical isogeometric Galerkin (SAIGA-G) and semi-analytical isogeometric collocation (SAIGA-C) for computing dispersion of guided-waves in anisotropic poroelastic plates immersed in acoustic fluids. Biot's theory was used for describing the dynamic behavior of anisotropic poroelastic material. Assuming the structures is homogeneous along its axial direction, the Non-Uniform Rational B-splines (NURBS) was successful employed in procedures using isogeometric Galerkin and collocation methods. The numeral studies showed that the SAIGA-G method using high continuity NURBS basis allowed to significantly improve the accuracy as well as the convergence rate of the wave dispersion solutions in compared with the conventional SAFE method, which used Lagrange basis functions. Otherwise, the SAIGA-C method was shown to have similar performance in terms of accuracy to the SAFE method.

Keywords: Guided-waves, anisotropic poroelasticity, wave dispersion, isogeometric analysis, NURBS basis, IGA collocation

1. Introduction

A poroelastic material consists of two phases, being the elastic solid phase and the fluid phase filling the pore spaces. Many materials encountered in civil, mechanical, geophysical and biomedical engineering can be considered as poroelastic media such as composites, rock, bone, etc. This work is concerned by studying the guided-wave propagation behavior in poroelastic media, which has a broad range of applications, for (non-exhaustive) example, the design of sound absorbing

materials [1, 2, 3] or the development of non-destructive testing (NDT) methods [4, 5, 6]. The wave propagation problem in poroelastic materials has been studied many investigations. When the dominant wavelengths of interests are sufficiently large with respect to the characteristic length of microscopic scale, Biot's and mixture theories were mostly employed [7], for which the governed dynamic equations are based on the displacement field of both solid and fluid phases.

Many analytical and numerical methods were developed for studying the propagation of guided-waves in poroelastic media. For example, Green's function of a homogeneous poroelastic halfspace may be found in [8, 9]. Transmission and reflection phenomena from poroelastic plate were carefully studied in many works [10, 11]. To study multi-layered poroelastic media, the dynamic stiffness method has been used for deriving the solutions in both frequency and time domains dynamic stiffness method [12, 13]. When the material properties are not piecewise-constant as in layered media but continuously varied, the asymptotic formulation using Peano's series has been developed [14, 15]. Although the analytical methods are generally fast, it has been shown that numerical instabilities may occur due to positive exponential terms for the cases of large layer thickness (in comparing with wavelengths in the medium), requiring some particular techniques [16, 17]. Moreover, analytical methods don't allow to consider the structures with complex geometries. Therefore, aside from developed analytical techniques, the so-called semi-analytical finite element method (SAFE) has been widely used. The core idea of SAFE method is to apply the Fourier transform along the direction in which the structure is assumed to be have infinite extent, and use FE discretization in its cross-section's plan. In many studies on visco-elastic waveguides, SAFE method has been shown to be very efficient for determining the primitive characteristics of dispersive guided waves (such as phase velocity, group velocities and attenuation), even when the coupling with surrounding fluids were considered [18, 19]. Using SAFE allows to easy handle the waveguides with functionally-graded properties [20, 21] or with arbitrary section's geometry [22, 23]. SAFE method was also successfully used for computing solutions of transient waves propagating in a anisotropic viscoelastic[24], poroelastic plates [25], multi-layered periodic piezoelectric composited plates [26] or thermo-acousto-elastic plates [27].

The accuracy of FE solution of wave propagation problems may be improved by employing smooth and higher-order basis functions. It has been shown that using higher-order FE methods (spectral element or p-FE) are efficient for the simulation of wave propagation in poroelastic layered

structures [28, 29, 30]. In some studies of guide-waves in elastic structures, spectral element methods (SEM) were also used. In [31], SAFE-SEM coupled with PML has been applied for modeling the leaky wave propagation in the embedded waveguides with cylindrical and square cross-section. Their results of convergence analysis show that the using high order SEM reduces the N_{dof} to achieve a given precision at the high frequency regime. Kalkowski et al. [32] recently used a SAFE-SEM formulation based on Gauss-Lobatto-Jacobi (GLJ) to examine buried and immersed fluid filled pipes. Although attractive features, the computational cost of SAFE for the estimation of high-frequency modes was still expensive because some extensive h- or p- refinements would be required. Moreover, when considering waveguides coupled with fluids, the mode shapes computed by SAFE may have some significant discontinuities at interfaces due to numerical errors of derivative approximation [33].

Isogeometric analysis (IGA) [34, 35], which uses the NURBS for the approximation of solutions fields, turned out to be very interesting technique as it exhibits increased accuracy and robustness in comparison to standard FE methods in the context of wave propagation simulation [36, 37]. In a recent work [33], NURBS basis functions was introduced within the SAFE framework and was shown to significantly increase the accuracy of dispersion curves of elastic guided waves in comparison to the standard SAFE method. Moreover, by employing this isogeometric-based approach (denoted by semi-analytical igeometric analysis - SAIGA), the continuity in mode shapes due the numerical errors at fluid-solid interfaces was much better described, even when simple geometry (plate-like) was considered. Using NURBS has also been shown to better describe the complex section's geometry and curvilinear interface between the solid and the fluid [38].

Although the NURBS-based discretization has been proposed for studying the guided-wave propagation in elastic media in numerous works [37, 39], its benefits when considering poroelastic media have not been investigated. For modeling poroelastic materials saturated by a fluid, the system of equations is more complex as it also includes the generalized Darcy's law, of which the resolution has usually numerical difficulties. Especially when the porosity is important and the problem is studied at high frequencies, the attenuation induced from interaction between the fluid and solid phases become much more significant and the robustness of numerical procedure for finding complex eigenvalues needs to be carefully investigated. In the literature, it has been shown that using IGA leads to a superior accuracy over FEA [40] for modeling static behavior of poroelastic

media,. In the dynamic context, Morganti et al. [41] presented an isogeometric collocation method for studying an 1D poroelastic wave propagation problem. The IGA collocation method [42] has been developed to combine the accuracy and the smoothness advantages of the IGA method with the computational efficiency of the collocation method. Since there are no volume integrals in the IGA collocation, the collocation methods is considerably cheaper from a computational point of view. Moreover, its implementation is simple, since one only need to evaluate the shape functions and the right-hand side data at chosen collocation points. The boundary conditions are imposed as additional constraints in the linear system, which is typically non-symmetric even for self-adjoint problem but more sparse as in the Galerkin method.

This paper aims to investigate the potential of isogeometric finite element methods for computing the dispersion of guided-waves in poroelastic media. We will focus on the studying the effectiveness of NURBS-based shape functions for the approximation of poroelastic equations in the context of guided waves analysis. To do so, we develop two semi-analytical procedures for solving the dispersion relation equations of guided waves in an anisotropic poroelastic plate immersed in acoustic fluids. The first one employs the isogeometric Galerkin method, which is based on the NURBS discretization of the weak formulation derived in the frequency-wavenumber domain to derive the eigenvalue (dispersion) system of equations. The second one uses the collocation isogeometric method, which based on an NURBS approximation of the strong form of the considered problem to derive the eigenvalue (dispersion) system of equations. To the best of authors' knowledge, the numerical performance of IGA-based methods for computing the dispersion curves of guided waves in poroelastic plates has not been studied in the literature.

The paper is organized as follows. Section 2 presents the equations (in strong and weak forms) describing wave propagation problem in coupled fluid-poroelastic system. According to the conventional semi-finite element method's framework, Section 3 presents the equations transformed into frequency-wavenumber domain. In Section 4, after introducing the main concepts of IGA, two methods of numerical resolution will be presented: (1) the semi-analytical isogeometric Galerkin (SAIGA-G) method, and (2) the semi-analytical isogeometric collocation (SAIGA-C) method. Section 5 subsequently carries out the validation and convergence analysis of the proposed methods through several examples. The paper will end with conclusive discussions in Section 6.

In the following, the symbol $\partial_i(\star)$ $(i = 1, 2)$ stands for the partial derivative of $(\star)$ with respect

to x_i; the symbol '$\cdot$' for the scalar product and the symbol ':' between tensors of any order for their double contraction; $\mathbf{a}^*$ stands for the conjugate transpose (or Hermitian transpose) of a matrix $\mathbf{a}$. Einstein summation convention is not used in this manuscript.

2. Problem statement

In this section, we will first describe the geometry of the fluid-solid coupled waveguide, then the equations (in both strong and weak forms) for modeling the wave propagation phenomena in the considered system.

2.1. Geometry description

Let us consider an anisotropic poroelastic layer (Ω^b) with infinite extents along $\mathbf{e}_1$-axis. The thicknessof the layer is assumed to be constant and is denoted by h. The surfaces of this layer may be stress-free or loaded by two surrounding fluid halfspaces. The domains occupied by the poroelastic layer and the fluids are denoted by $\Omega^b = \{(x_1, x_2) \in [-\infty, \infty] \times [0, h]\}$, $\Omega_1^f = \{(x_1, x_2) \in (-\infty, \infty) \times (-\infty, 0]\}$, $\Omega_2^f = \{(x_1, x_2) \in (-\infty, \infty) \times [h, +\infty)\}$, respectively. The interfaces between Ω and the fluid domains Ω_j^f are denoted by Γ_j^{bf} ($j = \{1, 2\}$), respectively. As the thickness is constant, the outward directed, normal vectors of Ω^b at Γ_1^{bf} and Γ_2^{bf} are given by $\boldsymbol{n}_1^b = \{0, -1\}^T$ and $\boldsymbol{n}_2^b = \{0, 1\}^T$, respectively.

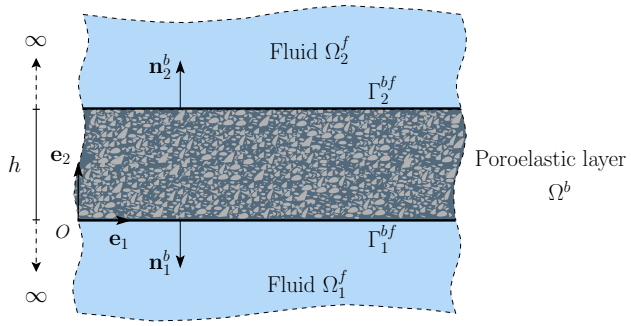

Figure 1: Schematic of a two-dimensional poroelastic waveguide coupled with fluid half-spaces

2.2. Gorverning equations

2.2.1. Wave equations in the fluids

The fluids occupying the domains Ω_j^f ($j = \{1, 2\}$) are modeled by an acoustic fluid whose mass density and bulk modulus at rest are denoted by K_j and ρ_j, respectively. The linearized wave and

Euler equations in fluids are expressed as follows:

$$\rho_j \ddot{p}_j - K_j \nabla^2 p_j = 0 \,, \tag{1}$$

$$\rho_j \dot{\boldsymbol{v}}_j + \nabla p_j = \mathbf{0} \,, \tag{2}$$

where p_j and $\boldsymbol{v}_j(\boldsymbol{x}, t)$ denote the acoustic pressure and velocity of fluids in Ω_j^f; $\nabla^2(\star)$ is the Laplace operator. The wave celerity in Ω_j^f can be defined by $c_j = \sqrt{K_j/\rho_j}$.

2.2.2. Dynamic equations in the poroelastic domain

The anisotropic poroelasticity theory is used to describe the behavior of porous domain (Ω^b). The poroelastic equations employed here are based upon Biot's original works [43, 44, 45] as well as the recent developments in anisotropic constitutive equations [46, 47, 48]. In Biot's theory the porous media is assumed to consist of a solid skeleton and a connected pore network saturated by fluid (with mass density ρ_f). The sealed pores are considered as part of the solid. It also assumes that the size of the pores is small compared to the characteristic wavelength, and applicability of continuum mechanics to macroscopic two-phase medium. At a point $\boldsymbol{x}$ and at time t, the vectors of displacement of the solid skeleton and of the interstitial fluid are denoted by $\boldsymbol{u}^s(\boldsymbol{x}, t)$ and $\boldsymbol{u}^f(\boldsymbol{x}, t)$, respectively; the relative displacement between the fluid and the solid frame weighted by the porosity ϕ is denoted by $\boldsymbol{w} = \phi(\boldsymbol{u}^f - \boldsymbol{u}^s)$. For the purpose of convenience, the Voigt's notation was used for representing the stress, strain and Biot's effective tensors under the vectorial forms as : $\boldsymbol{s}(\mathbf{x}, t) = \{\sigma_{11}, \sigma_{22}, \sigma_{12}\}^T$, $\boldsymbol{e}(\mathbf{x}, t) = \{\varepsilon_{11}, \varepsilon_{22}, 2\varepsilon_{12}\}^T$, $\boldsymbol{\alpha}(\mathbf{x}, t) = \{\alpha_{11}, \alpha_{22}, \alpha_{12}\}^T$, where σ_{ij}, ε_{ij} and α_{ij} are the components of the corresponding tensors. By using Voigt's notation, the Biot's constitutive equations for the anisotropic linear poroelastic material [49] read:

$$\boldsymbol{s} = \mathbf{C}\boldsymbol{e} - \boldsymbol{\alpha} p \,, \tag{3}$$

$$p = -M(\boldsymbol{m}^T \mathbb{L} \boldsymbol{w} + \boldsymbol{\alpha}^T \mathbb{L} \boldsymbol{u}^s) \,, \tag{4}$$

where p is the interstitial pore pressure; $\mathbf{C}_{3\times3}$ is the drained elastic tensor; the scalar M is the Biot's modulus; $\boldsymbol{m} = (1, 1, 0)^T$; and the operator $\mathbb{L}$ is defined by: $\mathbb{L} = \mathbf{L}_1\partial_1 + \mathbf{L}_2\partial_2$, in which $\mathbf{L}_1$ and $\mathbf{L}_2$ are 3×2 matrices whose the elements are zeros except the following ones: $L_1(1,1) = L_1(3,2) = L_2(2,2) = L_2(3,1) = 1$.

The wave propagation in the poroelastic medium is described by a system of two coupled equations representing the momentum equation and the dynamic Darcy law [50]. Neglecting the

body forces (other than inertia), this system reads:

$$\rho\ddot{\boldsymbol{u}}^s + \rho_f\ddot{\boldsymbol{w}} - \mathbb{L}^T\boldsymbol{s} = 0\ , \tag{5}$$

$$\rho_f\ddot{\boldsymbol{u}}^s + \tilde{\boldsymbol{a}} * \ddot{\boldsymbol{w}} + \mathbb{L}^T\boldsymbol{m}p = 0\ , \tag{6}$$

where $\rho = \phi\rho_f + (1-\phi)\rho_s$ is the mixture density (or apparent density); ρ_s and ρ_f are mass densities of the solid (matrix) material and the saturating fluid, respectively and ϕ is the porosity. The viscodynamic operator $\tilde{\boldsymbol{a}}$ is a frequency-dependent symmetric second-order tensor which depend on the permeability and tortuosity of the medium. For materials with orthorhombic symmetry, it has only non-zero diagonal components. In this work, we used the Johnson-Koplik-Dashen (JKD) model [51] in which the diagonal components of $\tilde{\boldsymbol{a}}$ are given by :

$$a_{jj}(\omega) = \frac{\rho_f}{\phi}\left(a_j^\infty + \frac{\mathrm{i}\phi\eta F_j(\omega)}{\omega\rho\kappa_j}\right)\ , \tag{7}$$

where, η denotes the dynamic viscosity of the pore fluid, a_j^∞ and κ_j are the tortuosity and the low-frequency limit permeability of the skeleton in the direction $\mathbf{e}_j$, respectively.

By noting that $\boldsymbol{e} = \mathbb{L}\boldsymbol{u}^s$ and by substituting Eq. (4) into Eq. (3), the vectors $\boldsymbol{s}$ and $\boldsymbol{m}p$ in Eqs. (5-6) may be expressed in terms of $\boldsymbol{u}^s$ and $\boldsymbol{w}$ as follows:

$$\boldsymbol{s} = \mathbf{C}_u\mathbb{L}\boldsymbol{u}^s + \mathbf{C}_\alpha\mathbb{L}\boldsymbol{w}\ , \tag{8}$$

$$\boldsymbol{m}p = -(\mathbf{C}_M\mathbb{L}\boldsymbol{w} + \mathbf{C}_\alpha^T\mathbb{L}\boldsymbol{u}^s)\ , \tag{9}$$

where $\mathbf{C}_u = \mathbf{C} + M\boldsymbol{\alpha}\boldsymbol{\alpha}^T$, $\mathbf{C}_\alpha = M\boldsymbol{\alpha}\boldsymbol{m}^T$, $\mathbf{C}_M = M\boldsymbol{m}\boldsymbol{m}^T$. The tensor $\mathbf{C}_u$ is known as the undrained elasticity tensor, which may be considered as the rigidity of an equivalent elastic medium in which the relative movement between the interstitial fluid and solid skeleton is null (*i.e.* when $\boldsymbol{w} = \mathbf{0}$). One may also notice that while $\mathbf{C}_u$ and $\mathbf{C}_M$ are symmetric, $\mathbf{C}_\alpha$ of an anisotropic medium is not; it could be symmetric only if the considered poroelastic medium is isotropic (*i.e.* when $\alpha_{11} = \alpha_{22}$ and $\alpha_{12} = 0$).

2.2.3. Boundary conditions

At interfaces between the porous media and the fluid domains. At both interfaces Γ_1^{bf} and Γ_2^{bf}, open pore condition was assumed, leading to a continuity condition of the normal velocity between the poroelastic medium and the surrounding fluids [50] :

$$\dot{\boldsymbol{w}}\cdot\mathbf{n}_j^b = (\boldsymbol{v}_j - \dot{\boldsymbol{u}}^s)\cdot\mathbf{n}_j^b\ , \quad \forall\boldsymbol{x}\in\Gamma_j^{bf}\ (j=\{1,2\}). \tag{10}$$

In view of the Euler equation (Eq. (2)), this interface condition may be rewritten as:

$$\left(\frac{1}{\rho_j}\nabla p_j + \ddot{\boldsymbol{w}} + \ddot{\boldsymbol{u}}^s\right)\cdot \mathbf{n}_j^b = 0\,, \quad \forall \boldsymbol{x} \in \Gamma_j^{bf}\ (j=\{1,2\}). \tag{11}$$

In addition, the conditions of stress continuity at the porous-fluid interfaces [50] impose that :

$$\left.\begin{array}{l} \boldsymbol{t} = -p_j \mathbf{n}_j^b \\ p = p_j \end{array}\right\} \quad \forall \boldsymbol{x} \in \Gamma_j^{bf}\ (j=\{1,2\}), \tag{12}$$

where $\boldsymbol{n}_j^b$ is the outward normal unit vector at the interfaces from Ω^b toward Ω_j^f and $\boldsymbol{t}$ is the traction vector. It is worth to note that the outward unit vector of the solid domain is related to unit vector of the fluid domain by $\mathbf{n}_j^b$=$-\mathbf{n}_j^f$ and $\boldsymbol{t} = \mathbf{L}_2^T\boldsymbol{s} = \{\sigma_{12}, \sigma_{22}\}^T$.

Exterior boundaries. The radiation condition of fluid pressure in Ω_j^f $(j=\{1,2\})$ may be formally written by :

$$p_j \to 0 \quad \text{when } |\boldsymbol{x}| \to \pm\infty, \tag{13}$$

2.3. Weak formulations

Weak formulation in the fluid domains. The pressure field in the fluid occupying the domain Ω_j^f is described by Eq. (1). The weak form of this equation by taking into account the boundary conditions Eqs. (13)-(11) reads

$$\int_{\Omega_j^f} \delta p_j^* \rho_j \ddot{p}_j d\Omega_j^f + \int_{\Omega_j^f} \nabla \delta p_j^* K_j \nabla p_j d\Omega_j^f - \int_{\Gamma_j^{bf}} \delta p_j^* \rho_j K_j (\ddot{\boldsymbol{u}}^s + \ddot{\boldsymbol{w}})\cdot \mathbf{n}_j^f d\Gamma_j^{bf} = 0\,, \quad \forall \delta p_j \in \mathcal{C}^{ad}, \tag{14}$$

Weak formulation in the poroelastic domain. Upon integrating Eqs. (5) and Eqs. (6) against the test function $\delta\boldsymbol{u}$ and $\delta\boldsymbol{w}$, respectively and considering the interface conditions Eqs. (13)-(11), the weak formulation of the boundary valued problem in the poroelastic layer Ω^b may be derived as:

$$\begin{aligned}
&\int_{\Omega^b} \delta\boldsymbol{u}^* \rho \ddot{\boldsymbol{u}}^s \mathrm{d}v + \int_{\Omega^b} \delta\boldsymbol{u}^* \rho_f \ddot{\boldsymbol{w}} \mathrm{d}v + \int_{\Omega^b} \mathbb{L}^T \delta\boldsymbol{u}^* (\mathbf{C}_u \mathbb{L}\boldsymbol{u}^s + \mathbf{C}_\alpha \mathbb{L}\boldsymbol{w}) \mathrm{d}v + \int_{\Gamma_j^{bf}} \delta\boldsymbol{u}^* \big(p_j \boldsymbol{n}^b\big) \mathrm{d}s = \mathbf{0}\,, \\
&\int_{\Omega^b} \delta\boldsymbol{w}^* (\tilde{\boldsymbol{a}} \ddot{\boldsymbol{w}}) \mathrm{d}v + \int_{\Omega^b} \delta\boldsymbol{w}^* \rho_f \ddot{\boldsymbol{u}}^s \mathrm{d}v + \int_{\Omega^b} \mathbb{L}^T \delta\boldsymbol{w}^* (\mathbf{C}_M \mathbb{L}\boldsymbol{w} + \mathbf{C}_\alpha^T \mathbb{L}\boldsymbol{u}^s) \mathrm{d}v + \int_{\Gamma_j^{bf}} \delta\boldsymbol{w}^* \big(p_j \boldsymbol{n}^b\big) \mathrm{d}s = \mathbf{0}\,, \\
&\forall (\delta\boldsymbol{u}, \delta\boldsymbol{w}) \in \mathcal{C}^{ad}.
\end{aligned} \tag{15}$$

3. Equations in the frequency-wavenumber domain

For studying the behavior of guided wave propagating along the longitudinal direction ($\mathbf{e}_1$) in the medium, we look for harmonic solutions for which a field φ ($\varphi \in \{u_1, u_2, w_1, w_2, p_1, p_2\}$) in Ω may be expressed under following form:

$$\varphi(x_1, x_2, t) = \tilde{\varphi}(x_2) e^{\mathrm{i}(k_1 x_1 - \omega t)} \ , \tag{16}$$

where $\mathrm{i}^2 = -1$; k_1 is the wavenumber in the $\mathbf{e}_1$-direction. Note that in the frequency-wavenumber $(\omega - k_1)$ domain, the derivatives with respect to t and to x_1 can be replaced by: $(\dot{\star}) \rightarrow -\mathrm{i}\omega(\star)$ and $\partial_1(\star) \rightarrow \mathrm{i}k_1(\star)$, respectively. Hence, the considered two-dimensional problem may be simplified into a system of one-dimensional (1D) PDEs with respect only to x_2. Moreover, in this study, as the semi-infinite fluid domains were modeled by using the well-known Perfect Matched Layer (PML) technique (see Appendix A), following finite 1D domains could be introduced $\bar{\Omega}^b = [0, h]$, $\bar{\Omega}^{f_1} = [-h_1^f, 0]$ and $\bar{\Omega}^{f_2} = [h, h + h_2^f]$ for modeling the poroelastic and fluid regions.

3.1. Strong form

By replacing Eq. (16) into Eqs. (1,5 & 6), the performing some algebraic manipulations, the later equations may be transformed into the $(\omega - k_1)$ domain as follows:

$$-\omega^2 \rho_j \tilde{p}_j + k_1^2 K_j \tilde{p}_j - K_j \partial_2^2 \tilde{p}_j = 0 \ , \quad \forall x_2 \in \bar{\Omega}_j^f, \quad j = \{1, 2\} \ , \tag{17}$$

$$-\omega^2 \mathbf{B}_\rho \mathbf{v} + k_1^2 \mathbf{B}_0 \mathbf{v} - \mathrm{i}k_1 (\mathbf{B}_1 + \mathbf{B}_1^T) \partial_2 \mathbf{v} - \mathbf{B}_2 \partial_2^2 \mathbf{v} = \mathbf{0}, \quad \forall x_2 \in \bar{\Omega}^b. \tag{18}$$

where $\mathbf{v} = (\tilde{\boldsymbol{u}}^s, \tilde{\boldsymbol{w}})^T$ and:

$$\mathbf{B}_\rho = \begin{bmatrix} \rho \mathbf{I}_2 & \rho_f \mathbf{I}_2 \\ \rho_f \mathbf{I}_2 & \tilde{\boldsymbol{a}} \end{bmatrix}, \quad \mathbf{B}_0 = \begin{bmatrix} \mathbf{A}_u^{11} & \mathbf{A}_\alpha^{11} \\ \mathbf{A}_\alpha^{11} & \mathbf{A}_M^{11} \end{bmatrix}, \quad \mathbf{B}_1 = \begin{bmatrix} \mathbf{A}_u^{12} & \mathbf{A}_\alpha^{12} \\ \mathbf{A}_\alpha^{12} & \mathbf{A}_M^{12} \end{bmatrix}, \quad \mathbf{B}_2 = \begin{bmatrix} \mathbf{A}_u^{22} & \mathbf{A}_\alpha^{22} \\ \mathbf{A}_\alpha^{22} & \mathbf{A}_M^{22} \end{bmatrix} \tag{19}$$

in which $\mathbf{I}_2$ denotes the 2-by-2 identity matrix; the matrices $\mathbf{A}_u^{ab}$, $\mathbf{A}_\alpha^{ab}$ and $\mathbf{A}_M^{ab}$ with $a, b = \{1, 2\}$ are defined by: $\mathbf{A}_u^{ab} = \mathbf{L}_a^T \mathbf{C}_u \mathbf{L}_b$, $\mathbf{A}_\alpha^{ab} = \mathbf{L}_a^T \mathbf{C}_\alpha \mathbf{L}_b$, $\mathbf{A}_M^{ab} = \mathbf{L}_a^T \mathbf{C}_M \mathbf{L}_b$.

The boundary conditions (Eqs. 11,13) for the fluid domains $\bar{\Omega}^{f_j}$ $(j = \{1, 2\})$ may be now expressed as:

$$\partial_2 \tilde{p}_j = \omega^2 \rho_j (\tilde{u}_2^s + \tilde{w}_2), \qquad \text{at } x_2 = x_2^{\Gamma_j^b}, \tag{20}$$

$$\tilde{p}_1 = \tilde{p}_2 = 0 \qquad \text{at } x_2 = x_2^{\Gamma_j^\infty} \tag{21}$$

where $x_2^{\Gamma_1^b}=0$, $x_2^{\Gamma_2^b}=h$, $x_2^{\Gamma_j^\infty}=-h_1^f$, $x_2^{\Gamma_2^\infty}=h+h_2^f$ are the vertical coordinates of fluid domains' boundaries, respectively. Similarly, the stress continuity conditions (Eq. 12) transformed into $(\omega-k_1)$ domain read:

$$\left.\begin{aligned} &\mathrm{i}k_1\left(\mathbf{A}_u^{21}\tilde{\boldsymbol{u}}+\mathbf{A}_u^{22}\tilde{\boldsymbol{w}}\right)+\left(\mathbf{A}_\alpha^{21}\partial_2\tilde{\boldsymbol{u}}+\mathbf{A}_\alpha^{22}\partial_2\tilde{\boldsymbol{w}}\right)=(0,-\tilde{p}_j)^T\\ &-\mathrm{i}k_1M\left(\alpha_{11}\tilde{u}_1+\alpha_{12}\tilde{u}_2+\tilde{w}_1\right)-M\left(\alpha_{12}\partial_2\tilde{u}_1+\alpha_{22}\partial_2\tilde{u}_2+\partial_2\tilde{w}_2\right)=\tilde{p}\end{aligned}\right\}\quad \text{at } x_2=x_2^{\Gamma_j^b} \tag{22}$$

3.2. Weak form

In the frequency-wavenumber domain, the weak formulations of the fluids ($\bar{\Omega}^{f_j},\ j=\{1,2\}$), and of the poroelastic layer ($\bar{\Omega}^b$) may be derived by replacing Eq. (16) into Eqs. (14,15):

$$\begin{aligned}&-\omega^2\int_{\bar{\Omega}_j^f}\delta\tilde{p}_j^*\rho_j\tilde{p}_j\gamma_2dx_2+k_1^2\int_{\bar{\Omega}_j^f}\delta\tilde{p}_j^*K_j\tilde{p}_j\gamma_2dx_2+\int_{\bar{\Omega}_j^f}\partial_2\delta\tilde{p}_j^*K_j\partial_2\tilde{p}_j(1/\gamma_2)dx_2\\ &\qquad-\omega^2\delta p_j^*\rho_jK_j\left(\tilde{u}_2^s(x_2^{\Gamma_j})+\tilde{w}_2(x_2^{\Gamma_j})\right)=0,\end{aligned} \tag{23}$$

$$\begin{aligned}&-\omega^2\int_{\bar{\Omega}^b}\delta\mathbf{v}\cdot\mathbf{B}_\rho\mathbf{v}dx_2+k_1^2\int_{\bar{\Omega}^b}\delta\mathbf{v}\cdot\mathbf{B}_0\mathbf{v}dx_2+\mathrm{i}k_1\int_{\bar{\Omega}^b}\left(\partial_2\delta\mathbf{v}\cdot\mathbf{B}_1\mathbf{v}-\delta\mathbf{v}\cdot\mathbf{B}_2\partial_2\mathbf{v}\right)dx_2\\ &\quad+\int_{\bar{\Omega}^b}\partial_2\delta\mathbf{v}\cdot\mathbf{B}_2\partial_2\mathbf{v}dx_2+(\delta\tilde{u}_2(0)+\delta\tilde{w}_2(0))\tilde{p}_1(0)+(\delta\tilde{u}_2(h)+\delta\tilde{w}_2(h))\tilde{p}_2(h)=0,\end{aligned} \tag{24}$$

in which $\gamma_2(x_2)$ is a continuous function which was introduced in the PMLs of the fluid domains (see Appendix A).

4. Numerical resolutions using NURBS-based approximations

In the framework of the conventional the semi-analytical finite element (SAFE) method, the Lagrange polynomials may be used for the approximation of the Eqs. (23)-(24). To do so, it is well known that a sufficient number of grid points per wavelength has to be adjusted, to be able to capture the oscillation of the solution. Thus, the quality of numerical solutions depends on the wave-number k_1. It has also been shown that for large wave-number problems, using high-order interpolation polynomials would be better to reduce the numerical errors than using lower-order ones with refined element sizes. In this section, we propose to use the high-order interpolation based on NURBS for improve computational efficiency on determining the wave dispersion in high-frequency. The idea is based on the NURBS-based isogeometric analysis allowing the use of globally C^k-continuous basis functions, with $k\leq p-1$, p being the polynomial degree. In this section, we firstly briefly recall the concept of isogeometric analysis with the main focus on

the B-spline and NURBS basis functions. Next, we develop two numerical approaches based on isogeometric Galerkin and collocation methods to compute the dispersion of guided-waves in anisotropic poroelastic plates immersed in fluids.

4.1. B-spline and NURBS basis functions

In the framework of standard SAFE method, Lagrange polynomials usually served as interpolation functions for the discretization of weak formulations presented in Sec. 3.2. In this paper, we adopt isogeometric-based approaches where the NURBS basis functions are used for discretizing the problems (in strong or weak forms) presented in Sec. 3. Basically, B-spline basis functions of order q are determined in a parameter domain $\hat{\Omega} \subset \mathbb{R}$ using a sequence of non-decreasing set of coordinates called *knot vector* defined as $\Xi = \{\xi_1, \xi_2, \xi_3, ..., \xi_{n+q+1}\}$, where $\xi_i \in \mathbb{R}$ $(i = 1, 2, ..., n)$ is the i^{th} knot and n is the number of basis functions used to construct the B-spline curve. For a given knot vector, the corresponding set of B-spline basis functions $B_{i,q}$ are defined by the well-known Cox-de Boor recursion formula as:

$$q = 0 \ : \quad B_{i,0}(\xi) = \begin{cases} 1 & \text{if } \xi_i < \xi < \xi_{i+1}, \\ 0 & \text{otherwise,} \end{cases} \tag{25a}$$

$$q > 0 \ : \quad B_{i,q}(\xi) = \frac{\xi - \xi_i}{\xi_{i+q} - \xi_i} B_{i,q-1}(\xi) + \frac{\xi_{i+q+1} - \xi}{\xi_{i+q+1} - \xi_{i+1}} B_{i+1,q-1}(\xi). \tag{25b}$$

Note that the quotient $0/0$ is assumed to be zero. Open knot vectors, where the first and the last knot each have a multiplicity of $q+1$, are standard in CAD NURBS basis functions are built from the B-spline functions by assigning a weigh w_i to every B-spline function $B_{i,q}(\xi)$:

$$R_{i,q}(\xi) = \frac{B_{i,q}(\xi) w_i}{\sum_{j=1}^{n} B_{j,q}(\xi) w_j}. \tag{26}$$

The NURBS basis functions have some advantage such as higher continuity across the element boundaries, partition of unity, variation diminishing, linear independence and compact support. Such a complete set of basis functions can be employed in any finite finite element or collocation framework. According to the isogeometric concept in which the same basis functions are used for the approximation of solution fields and for geometry representation, the approximation of a complex-valued function $\varphi(x)$, denoted by $\hat{\varphi}^h$, is given by :

$$\varphi(x) \approx \hat{\varphi}^h = \sum_{i=1}^{n} R_{i,q}(\xi) \Phi_i \ , \tag{27}$$

where the complex-valued coefficients Φ_i are the corresponding control variables (values at the control points). Using the inversion of geometrical mapping $x_2(\xi)$ the function $\hat{v}^h$ over the physical domain Ω can be define such that $v^h = \hat{v}^h \circ x^{-1}$.

4.2. Semi-analytical isogeometric Galerkin method (SAIGA-G)

For simplify the presentation, we assume that each domain $\bar{\Omega}_1^f$, $\bar{\Omega}_2^f$ and $\bar{\Omega}^b$ is discretized using only one patch with n_1, n_b, n_2 being the number of basis functions in the patches of $\bar{\Omega}^{f_1}$, $\bar{\Omega}^b$, $\bar{\Omega}^{f_2}$, respectively. By using the Galerkin finite element method, same approximations are applied for both functions $\tilde{\boldsymbol{u}}^h$ and $\delta\tilde{\boldsymbol{u}}^h$ (as well as for $\tilde{\boldsymbol{w}}^h$ and $\delta\tilde{\boldsymbol{w}}^h$; $\tilde{p}_\alpha^h$ and $\delta\tilde{p}_\alpha^h$) on each patch:

$$\tilde{\boldsymbol{u}}^h = \mathbf{R}^u\mathbf{U}, \quad \delta\tilde{\boldsymbol{u}}^h = \mathbf{R}^u\delta\mathbf{U}, \tag{28a}$$

$$\tilde{\boldsymbol{w}}^h = \mathbf{R}^w\mathbf{W}, \quad \delta\tilde{\boldsymbol{w}}^h = \mathbf{R}^w\delta\mathbf{W}, \tag{28b}$$

$$\tilde{p}_j^h = \mathbf{R}_j^p\mathbf{P}_j, \quad \delta\tilde{p}_j^h = \mathbf{R}_j^p\delta\mathbf{P}_j, \tag{28c}$$

where $\mathbf{R}^u_{2\times 2n_b}$, $\mathbf{R}^w_{2\times 2n_b}$ and $(\mathbf{R}^p_j)_{1\times n_j}$ are the interpolation matrix containing the NURBS basis functions (Eq. (26)); $\mathbf{U}_{2n_b\times 1}$, $\delta\mathbf{U}_{2n_b\times 1}$, $\mathbf{W}_{2n_b\times 1}$ and $\delta\mathbf{W}_{2n_b\times 1}$ are the vectors of control displacements; $(\mathbf{P}_j)_{n_j\times 1}$ and $(\delta\mathbf{P}_j)_{n_j\times 1}$ are the pressure vectors of control pressures. In this work, we used the same NURBS basis functions for approximation of the solution fields in Eqs. (28a-28c). By substituting the approximations (Eqs. 28a-28c) into the weak formulations (Eqs. 23-24), one obtains a eigenvalue problem:

$$(-\omega^2\mathbf{M} + \mathbf{K}_0 + \mathrm{i}k_1\mathbf{K}_1 + k_1^2\mathbf{K}_2)\mathbf{V} = \mathbf{0}\ , \tag{29}$$

where $\mathbf{V} = (\mathbf{P}_1, \mathbf{U}, \mathbf{W}, \mathbf{P}_2)^T$ contains the global eigenvectors the fluid pressures ($\mathbf{P}_1$, $\mathbf{P}_2$) in fluids and of displacements ($\mathbf{U}$, $\mathbf{W}$) in the poroelastic domain, respectively; the global matrices $\mathbf{M}$ and $\mathbf{K}_0$, $\mathbf{K}_1$, $\mathbf{K}_2$ are are square matrices of order $(n_1 + 4n_b + n_2)$ and may be determined from the

assembling of corresponding elementary matrices in poroelastic and fluid domains:

$$\mathbf{M}=\begin{bmatrix}\mathbf{M}^{p_1} & \mathbf{M}^{p_1u} & \mathbf{M}^{p_1w} & \mathbf{0}\\ \mathbf{0} & \mathbf{M}^{u} & \mathbf{M}^{uw} & \mathbf{0}\\ \mathbf{0} & \mathbf{M}^{wu} & \mathbf{M}^{w} & \mathbf{0}\\ \mathbf{0} & \mathbf{M}^{p_2u} & \mathbf{M}^{p_2w} & \mathbf{M}^{p_2}\end{bmatrix},\mathbf{K}_0=\begin{bmatrix}\mathbf{K}_0^{p_1} & \mathbf{0} & \mathbf{0} & \mathbf{0}\\ \mathbf{K}_0^{up_1} & \mathbf{K}_0^{u} & \mathbf{K}_0^{uw} & \mathbf{K}_0^{up_2}\\ \mathbf{K}_0^{wp_1} & \mathbf{K}_0^{wu} & \mathbf{K}_0^{w} & \mathbf{K}_0^{wp_2}\\ \mathbf{0} & \mathbf{0} & \mathbf{0} & \mathbf{K}_0^{p_2}\end{bmatrix}, \tag{30a}$$

$$\mathbf{K}_1=\begin{bmatrix}\mathbf{0} & \mathbf{0} & \mathbf{0} & \mathbf{0}\\ \mathbf{0} & \mathbf{K}_1^{u} & \mathbf{K}_1^{uw} & \mathbf{0}\\ \mathbf{0} & \mathbf{K}_1^{wu} & \mathbf{K}_1^{w} & \mathbf{0}\\ \mathbf{0} & \mathbf{0} & \mathbf{0} & \mathbf{0}\end{bmatrix},\mathbf{K}_2=\begin{bmatrix}\mathbf{K}_2^{p_1} & \mathbf{0} & \mathbf{0} & \mathbf{0}\\ \mathbf{0} & \mathbf{K}_2^{u} & \mathbf{K}_2^{uw} & \mathbf{0}\\ \mathbf{0} & \mathbf{K}_2^{wu} & \mathbf{K}_2^{w} & \mathbf{0}\\ \mathbf{0} & \mathbf{0} & \mathbf{0} & \mathbf{K}_2^{p_2}\end{bmatrix}, \tag{30b}$$

In these matrices, the sub-matrices related to the poroelastic solution fields $(\mathbf{U},\mathbf{W})$ and fluid pressure fields $(\mathbf{P}_1,\mathbf{P}_2)$ may be distinguished. For the poroelastic layer, the matrices related to the $\mathbf{U}$ are defined as:

$$\mathbf{M}^{u}=\int_{\bar{\Omega}^b}(\mathbf{R}^u)^T\rho\mathbf{R}^u dx_2,\quad \mathbf{M}^{uw}=\int_{\bar{\Omega}^b}(\mathbf{R}^u)^T\rho_f\mathbf{R}^w dx_2\ , \tag{31a}$$

$$\mathbf{K}_2^{u}=\int_{\bar{\Omega}^b}(\mathbf{R}^u)^T\mathbf{A}_u^{11}\mathbf{R}^u dx_2,\quad \mathbf{K}_2^{uw}=\int_{\bar{\Omega}^b}(\mathbf{R}^u)^T\mathbf{A}_\alpha^{11}\mathbf{R}^w dx_2\ , \tag{31b}$$

$$\mathbf{K}_1^{u}=\int_{\bar{\Omega}^b}2\left\{(\partial_2\mathbf{R}^u)^T\mathbf{A}_u^{21}\mathbf{R}^u\right\}_a dx_2\ ,\quad \mathbf{K}_1^{uw}=\int_{\bar{\Omega}^b}2\left\{\partial_2(\mathbf{R}^u)^T\mathbf{A}_\alpha^{21}\mathbf{R}^w\right\}_a dx_2\ , \tag{31c}$$

$$\mathbf{K}_0^{u}=\int_{\bar{\Omega}^b}\partial_2(\mathbf{R}^u)^T\mathbf{A}_u^{22}\partial_2\mathbf{R}^u dx_2,\quad \mathbf{K}_0^{uw}=\int_{\bar{\Omega}^b}\partial_2(\mathbf{R}^u)^T\mathbf{A}_\alpha^{22}\partial_2\mathbf{R}^w dx_2\ , \tag{31d}$$

$$\left(\mathbf{K}_0^{up_1}\right)_{\ell k}=\delta_{\ell 2}\delta_{kn_1},\quad \left(\mathbf{K}_0^{up_2}\right)_{\ell k}=\delta_{\ell(2n_b)}\delta_{k1}, \tag{31e}$$

where $\{\cdot\}_a$ denotes the anti-symmetric part of a matrix; δ_{jk} denotes the Kronecker's delta; the upper indexes ^{uw} or ^{up} represent the couplings between $\mathbf{U}$ & $\mathbf{W}$ or $\mathbf{U}$ & $\mathbf{P}_j$, respectively. Similarly, the matrices related to the $\mathbf{W}$ are given by :

$$\mathbf{M}^{w}=\int_{\bar{\Omega}^b}(\mathbf{R}^w)^T\tilde{\boldsymbol{a}}\mathbf{R}^w dx_2\ ,\quad \mathbf{M}^{wu}=\int_{\bar{\Omega}^b}(\mathbf{R}^w)^T\rho_f\mathbf{R}^u dx_2\ , \tag{32a}$$

$$\mathbf{K}_2^{w}=\int_{\bar{\Omega}^b}(\mathbf{R}^w)^T\mathbf{A}_M^{11}\mathbf{R}^w dx_2\ ,\quad \mathbf{K}_2^{wu}=\int_{\bar{\Omega}^b}(\mathbf{R}^w)^T\mathbf{A}_\alpha^{11}\mathbf{R}^u dx_2\ , \tag{32b}$$

$$\mathbf{K}_1^{w}=\int_{\bar{\Omega}^b}2\left\{(\partial_2\mathbf{R}^w)^T\mathbf{A}_M^{21}\mathbf{R}^w\right\}_a dx_2\ ,\quad \mathbf{K}_1^{wu}=\int_{\bar{\Omega}^b}2\left\{(\partial_2\mathbf{R}^w)^T\mathbf{A}_\alpha^{21}\mathbf{R}^u\right\}_a dx_2\ , \tag{32c}$$

$$\mathbf{K}_0^{w}=\int_{\bar{\Omega}^b}(\partial_2\mathbf{R}^w)^T\mathbf{A}_M^{22}\partial_2\mathbf{R}^w dx_2\ ,\quad \mathbf{K}_0^{wu}=\int_{\bar{\Omega}^b}(\partial_2\mathbf{R}^w)^T\mathbf{A}_\alpha^{22}\partial_2\mathbf{R}^u dx_2\ , \tag{32d}$$

$$\left(\mathbf{K}_0^{wp_1}\right)_{\ell k}=\delta_{\ell(2n_b+2)}\delta_{kn_1},\quad \left(\mathbf{K}_0^{wp_2}\right)_{\ell k}=\delta_{\ell(4n_b)}\delta_{k1},\ , \tag{32e}$$

where the upper indexes ^{wu} or ^{wp} represent the couplings between $\mathbf{W}$ & $\mathbf{U}$ or $\mathbf{W}$ & $\mathbf{P}_j$, respectively. The matrices related to the $\mathbf{P}_1$ and $\mathbf{P}_2$ are defined as:

$$\mathbf{M}^{p_j} = \int_{\bar{\Omega}} \rho_j \gamma_{2j} (\mathbf{R}_j^p)^T \mathbf{R}_j^p dx_2, \tag{33a}$$

$$\mathbf{K}_0^{p_j} = \int_{\bar{\Omega}} (K_j/\gamma_{2j}) (\partial_2 \mathbf{R}_j^p)^T \partial_2 \mathbf{R}_j^p dx_2, \quad \mathbf{K}_2^{p_j} = \int_{\bar{\Omega}} K_j \gamma_{2j} (\mathbf{R}^p)^T \mathbf{R}^p dx_2, \tag{33b}$$

$$\left(\mathbf{M}^{p_1 u}\right)_{\ell k} = \rho_1 K_1 \delta_{\ell(n_1)} \delta_{k2}, \quad \left(\mathbf{M}^{p_1 w}\right)_{\ell k} = \rho_1 K_1 \delta_{\ell(n_1)} \delta_{k(2n_b+2)}, \tag{33c}$$

$$\left(\mathbf{M}^{p_2 u}\right)_{\ell k} = \rho_2 K_2 \delta_{\ell 1} \delta_{k(2n_b)}, \quad \left(\mathbf{M}^{p_2 w}\right)_{\ell k} = \rho_2 K_2 \delta_{\ell 1} \delta_{k(4n_b)} \tag{33d}$$

Further more due to the fact that $\mathbf{A}_{\alpha\beta} = \mathbf{A}_{\beta\alpha}^T$, it can be shown that that the sub-matrices of the $\mathbf{M}$, $\mathbf{K}_0$, $\mathbf{K}_2$ are symmetric while the sub-matrices of $\mathbf{K}_1$ is anti-symmetric. Note that the in the case where there is no fluid half-spaces the fluid contribution and the corresponding coupling matrices are zeros matrices. All these sub-matrices are computed by using Gauss–Legendre quadrature formula with $r = q + 1$ quadrature nodes per element along each parametric direction which has been shown to be efficient [52].

4.3. Semi-analytical isogeometric collocation (SAIGA-C)

To construct the 1D isogeometric collocation method, we follow [42] by firstly choosing three sets of collocation points $\tau_i^{f_1}$ $(i = 1, .., n_1^{\text{col}})$, τ_j^b $(j = 1, .., n_b^{\text{col}})$ and $\tau_k^{f_2}$ $(k = 1, .., n_2^{\text{col}})$ for $\bar{\Omega}^{f_1}$, $\bar{\Omega}^{f_2}$ and $\bar{\Omega}^b$, respectively. Then we seek the approximations of the fields $\tilde{p}_1$, $\tilde{p}_2$, $\tilde{\boldsymbol{u}}$, $\tilde{\boldsymbol{w}}$ at the collocation points by using the associated NURBS basis functions. In this study, the employed collocation points (τ_i^{φ}) of a field φ $(\varphi = \{u_1, u_2, w_1, w_2, p_1, p_2\})$ are located at the images of the so-called "Greville abscissa". In general, using a given open knot vector $\Xi = \{\xi_1 = 0, \xi_2, \xi_3, ..., \xi_{n+q+1} = 1\}$, in which the first and the last knots have multicity $q + 1$, the Greville abscissae points $\bar{\xi}_i$ $(i = 1, 2, ..., n)$ in a parametric space are calculated by

$$\bar{\xi}_i = \frac{\xi_{i+1} + \xi_{i+2} + ... + \xi_{i+q}}{q}. \tag{34}$$

By building matrices which contain the k-th derivatives $(k = 0, 1, 2)$ of the NURBS shape functions of the field φ at all collocation points (τ_i^{φ}), the k-th derivatives of φ may be approximated by

(Eq. 26)

$$\begin{pmatrix} \partial_2^{(k)}\varphi(\tau_1^{\varphi}) \\ \partial_2^{(k)}\varphi(\tau_2^{\varphi}) \\ \vdots \\ \partial_2^{(k)}\varphi(\tau_{n_\varphi^{\mathrm{col}}}^{\varphi}) \end{pmatrix} \approx \begin{bmatrix} \partial_2^{(k)}R_1^{\varphi}(\tau_1^{\varphi}) & \partial_2^{(k)}R_2^{\varphi}(\tau_1^{\varphi}) & \cdots & \partial_2^{(k)}R_{n_\varphi^{\mathrm{col}}}^{\varphi}(\tau_1^{\varphi}) \\ \partial_2^{(k)}R_1^{\varphi}(\tau_2^{\varphi}) & \partial_2^{(k)}R_2^{\varphi}(\tau_2^{\varphi}) & \cdots & \partial_2^{(k)}R_{n_\varphi^{\mathrm{col}}}^{\varphi}(\tau_2^{\varphi}) \\ \cdots & \cdots & \cdots & \cdots \\ \partial_2^{(k)}R_1^{\varphi}(\tau_{n_\varphi^{\mathrm{col}}}^{\varphi}) & \partial_2^{(k)}R_1^{\varphi}(\tau_{n_\varphi^{\mathrm{col}}}^{\varphi}) & \cdots & \cdots \partial_2^{(k)}R_{n_\varphi^{\mathrm{col}}}^{\varphi}(\tau_{n_\varphi^{\mathrm{col}}}^{\varphi}) \end{bmatrix} \begin{pmatrix} \Phi_1 \\ \Phi_2 \\ \vdots \\ \Phi_{n_\varphi^{\mathrm{col}}} \end{pmatrix}, \tag{35}$$

where Φ_i denotes the solution of $\varphi(\tau_i^{\varphi})$ at the control points.

In the fluid domain $\bar{\Omega}_j^f$ $(j = 1, 2)$, giving a set of collocation points $\tau_i^{f_j}$ $(i = 1, ..., n_j^{\mathrm{col}})$, one may *a priori* derive from (Eq. (17)) a system of (n_j^{col}) equations at every collocations points:

$$-\omega^2\rho_j\tilde{p}_j(\tau_i^{f_j}) + k_1^2K_j\tilde{p}_j(\tau_i^{f_j}) - K_j\partial_2^2\tilde{p}_j(\tau_i^{f_j}) = 0\,. \tag{36}$$

However, as this system should satisfy the boundary conditions (20), two equations at the first and last collocation points should be replaced, for instance in the lower fluid domain $\bar{\Omega}_1^f$, by:

$$\tilde{p}_1(\tau_1^{f_1}) = 0, \tag{37}$$

$$\partial_2\tilde{p}_1(\tau_{n_1^{\mathrm{col}}}^{f_1}) + \rho_1\omega^2\left(\tilde{u}_2(\tau_1^b) + \tilde{w}_2(\tau_1^b)\right) = 0. \tag{38}$$

Similar conditions may be set for the upper fluid domain $\bar{\Omega}_2^f$.

Considering the poroelastic domain $\bar{\Omega}^b$, the approximate solutions $\tilde{\boldsymbol{u}}$ and $\tilde{\boldsymbol{w}}$ are evaluated at the collocation points τ_i^b $(i = 1, ..., n_b^{\mathrm{col}})$ should satisfy (18):

$$-\omega^2\mathbf{B}_\rho\mathbf{v}(\tau_i^b) + k_1^2\mathbf{B}_0\mathbf{v}(\tau_i^b) - \mathrm{i}k_1(\mathbf{B}_1 + \mathbf{B}_1^T)\partial_2\mathbf{v}(\tau_i^b) - \mathbf{B}_2\partial_2^2\mathbf{v}(\tau_i^b) = \mathbf{0}, \tag{39}$$

At the Γ_1^{bf} (interface between Ω_1^f and Ω^b), the stress continuity conditions (22) may be expressed in matrix form as follows:

$$\mathrm{i}k_1\begin{bmatrix} \mathbf{A}_u^{21} & \mathbf{A}_u^{22} \\ [M\alpha_{11}, M\alpha_{12}] & [1, 0] \end{bmatrix}\mathbf{v}(\tau_1^b) + \begin{bmatrix} \mathbf{A}_\alpha^{21} & \mathbf{A}_\alpha^{22} \\ [M\alpha_{12}, M\alpha_{22}] & [0, 1] \end{bmatrix}\partial_2\mathbf{v}(\tau_1^b) = -\begin{pmatrix} 0 \\ 1 \\ 1 \end{pmatrix}\tilde{p}_1(\tau_{n_1^{\mathrm{col}}}^{f_1}) \tag{40}$$

Again, a similar condition may be set at the interface Γ_2^{bf}.

By applying the approximations (35) to the Eqs. (36-40), then performing some algebraic manipulations for assembling the matrices, we can establishing a eigenvalue system containing

$n_1^{\text{col}} + 4 \times n_b^{\text{col}} + n_2^{\text{col}}$ equations which has the same form as the one derived by SAIGA-G procedure (Eq. (29)):

$$(\mathbf{K}_0 + \mathrm{i}k_1\mathbf{K}_1 + k_1^2\mathbf{K}_2 - \omega^2\mathbf{M})\mathbf{V} = \mathbf{0}\ , \tag{41}$$

4.4. Resolution of dispersion equations

The system of characteristic equations (29) and (41) are an eigenvalue problem which are used to determine the relationship between the pulsation ω and the wavenumber k_1. By noting that all global matrices $\mathbf{K}_0$, $\mathbf{K}_1$, and $\mathbf{K}_2$ do not depend on k_1, Eqs. (29) and (41) are a quadratics eigenvalue problem with respect to k_1 and could be solved by reformulating them under following linearized eigenvalue problem:

$$\left(\begin{bmatrix} \mathbf{0} & -\omega^2\mathbf{M} + \mathbf{K}_0 \\ -\omega^2\mathbf{M} + \mathbf{K}_0 & \mathrm{i}\mathbf{K}_1 \end{bmatrix} - k_1 \begin{bmatrix} -\omega^2\mathbf{M} + \mathbf{K}_0 & \mathbf{0} \\ \mathbf{0} & -\mathbf{K}_2 \end{bmatrix} \right) \begin{pmatrix} \mathbf{V} \\ k_1\mathbf{V} \end{pmatrix} = \mathbf{0}\ . \tag{42}$$

For each value of the angular frequency ω, solving Eq. (42) allows us to determine the eigenvalues k_1 and their associated eigenvectors (also called by wave structures), $\mathbf{V}(\omega, k_1)$ of guided modes. The frequency-dependent phase velocity ($C_{\text{ph}}(\omega)$) and the attenuation ($\gamma(\omega)$) of a guided mode are given by:

$$C_{\text{ph}} = \frac{\omega}{\mathsf{Re}(k_1)}\ [\text{m.s}^{-1}], \quad \gamma = \mathsf{Im}(k_1)\ [\text{Np.m}^{-1}]\ , \tag{43}$$

where $\mathsf{Re}()$ and $\mathsf{Im}()$ denote the real and imaginary parts of a complex function.

5. Numerical examples

In this section, we will investigate the performance of the proposed NURBS-based methods (*i.e* SAIGA-C and SAIGA-G methods) for computing the dispersion of poroelastic guided-waves in free and fluid coupled anisotropic poroelastic layers. For all examples, the evaluation of the phase velocities, the attenuations as well the mode shapes have been performed by using three approaches SAIGA-C, SAIGA-G and conventional SAFE. As the closed form of analytical solutions are not available, the SAFE's solutions obtained by very fine meshes, which are assumed to be the converged solutions, are served as the reference ones for estimating the numerical errors.

5.1. *Case of free-boundaries homogeneous poroelastic layers*

5.1.1. *Reference solutions*

We consider a 4-mm-thick saturated anisotropic poroelastic plate, which represents a typical cortical bone sample [25]. The porous bone material is assumed to be saturated by water of which the bulk modulus is $K_f = 2.5$ GPa and the density is $\rho_f = 1000$ kg.m^{-3}. The bone's matrix has a density $\rho_s = 1772$ kg.m^{-3} and its components of the elastic tensor (using the Voigt's notations) are given by : $c_{11}^m = 28.7$ GPa, $c_{22}^m = 23.6$ GPa, $c_{12}^m = 9.9$ GPa, $c_{66}^m = 7.25$ GPa and $c_{16}^m = c_{26}^m = 0$ GPa. By using the procedure presented in Appendix B, one can estimate the components of the drained elastic tensor $\mathbf{C}$. For example, the components of $\mathbf{C}$ are given in Tab. 5.1.1 for the porosity of $\phi = 0.1$ and $\phi = 0.5$. In this numerical study, we assume that the permeability an the tortuosity in the considered medium are isotropic. The diagonal terms of the tortuosity tensor is given by: $a_{11} = a_{22} = 1$.

Table 1: Parameters of the poroelastic medium for different values of the porosity.

ϕ	c_{11}	c_{12}	c_{22}	c_{66}	$c_{16} = c_{26}$	M	$\kappa_{11} = \kappa_{22}$
-	(GPa)	(GPa)	(GPa)	(GPa)	(GPa)	(GPa)	(m^2)
0.1	24.84	7.27	17.5	5.49	0	18.32	3.33×10^{-13}
0.5	12.76	2.33	5.71	1.87	0	4.19	1.67×10^{-12}

We first present in Figs. 2(a,b) the results of the phase velocity and attenuation computed by using the conventional SAFE formulation with a very fine mesh ($N_{\text{dof}} = 404$ and $q = 2$), which would be sufficient to be considered as a reference solutions. Due to the presence of fluid-filled pores, there exist some guided-wave modes with high attenuation. In Fig. 2(a,b), the dispersion curves are displayed in two different colors for separated the "low attenuation" (group 1) and "high attenuation" (group 2) modes, which have attenuation ($\gamma = \mathsf{Im}(k_1)$) greater or smaller than a value $\bar{\gamma} = 100$ m^{-1}, respectively. The phase velocity curves of low-attenuation modes (Fig. 2a) are similar to the well-known Lamb-type modes in elastic plates, which are usually designated by the modes A or the modes S in depending to their antisymmetric/symmetric natures. For these modes, the relative fluid-solid displacement ($\boldsymbol{w}$), which is the main cause of viscous effect in poroelastic materials, are much weaker than the displacements of the solid ($\boldsymbol{u}$). As an illustration,

Fig. 3(a) depicts the shape modes of u_2 and w_2 of the mode A_1 at the frequency $f = 1$ MHz, in which w_2 is found much smaller than u_2. Moreover, for this anti-symmetric mode, one may check that $u_2(0) = u_2(h)$ and $w_2(0) = w_2(h)$ with one wavelength over the plate thickness. Figs. 3(b,c) present the in-depth variation of u_2 and w_2 of two high attenuated modes, which correspond to two points B and C at the same frequency ($f = 1\ MHz$) as marked in Fig. 2. One may observe that the orders of these modes are higher with more wavelengths over the thickness. Moreover, the fluid-solid relative displacement becomes more significant in comparing to the solid displacement u_2, which induce more important attenuation as expected.

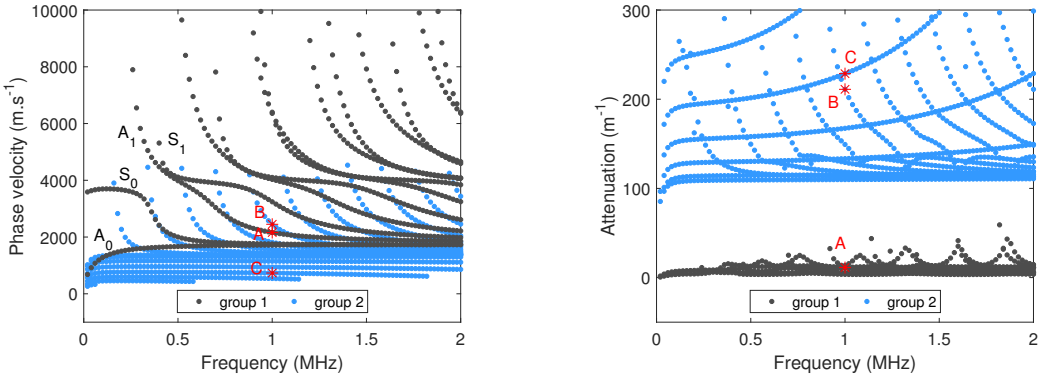

(a) phase velocity ($\omega/\mathsf{Re}(k_1)$) (b) attenuation ($\mathsf{Im}(k_1)$)

Figure 2: Dispersion curves (a) phase velocity versus frequency and (b) attenuation versus frequency of a free poroelastic bone layer; groups 1 and 2 represent low and high attenuated waves, respectively; a filtering criteria $\bar{\gamma} = 100$ m^{-1}

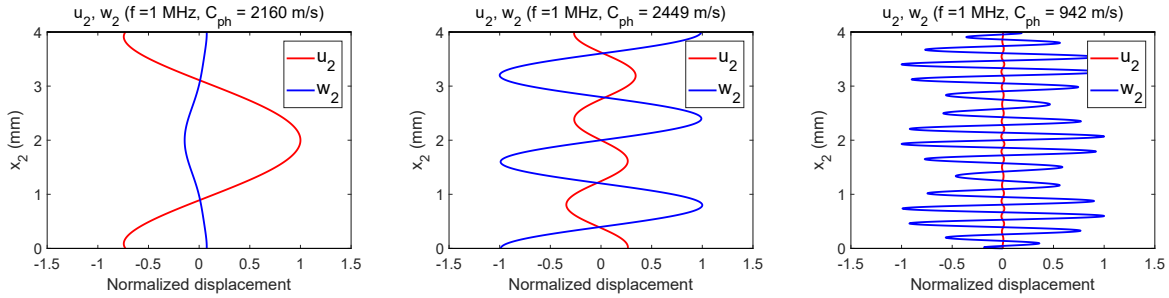

(a) low att. mode (point A) (b) high att. mode (point B) (c) high att. mode (point C)

Figure 3: (Color online) (u_2, w_2) shape modes corresponding to the points (A),(B),(C) marked in Fig. 2

The wave dispersion in poroelastic plates depends on its porosity [53]. In Fig. 4, the phase velocity (C_{ph}) and attenuation (γ) of the first symmetric mode S_0 are shown to be strongly modified while the porosity changes. To visualize the effect of porosity on the wave dispersion, we present in Fig. 4(a) the variation of real and imaginary parts of the wavenumber (k_1) *versus* frequency in a 3D graph. Different to the case of elastic plates in which the real wavenumber solutions exist, the wavenumbers of guided-waves poroelatic plates are complex. When $\phi = 0.1$, $\mathsf{Im}(k_1)$ is small even at high frequency and the k_1-curve is found closely to the plane $\omega - \mathsf{Re}(k_1)$. The peaks of the attenuation curves may be observed at frequencies where higher modes are cut-on. When $\phi = 0.5$, the imaginary part $\mathsf{Im}(k_1)$ was found to be much higher because the viscous effect due to fluid-solid relative movement becomes more significant, especially at high frequency. In high frequency range ([1.5-2.0] MHz), the phase velocity of S_0-mode tends to the Rayleigh wave's velocity (let us denote it by c_R), which depend mainly to the porosity and to components of drained elasticity tensor. As it has been shown in [54], the ratio c_R^2/c_{66} is monotonically increasing function with respect to the porosity. However, the shear modulus c_{66} (estimated by using the model presented in Appendix B) was found to be a monotonically decreasing function with respect to the porosity (see Table 1). Hence, in contrast with the attenuation which depends on the permeability and typically increases with higher porosity, varying the porosity may lead to insignificant change of the S_0-mode's phase velocity at high frequencies.

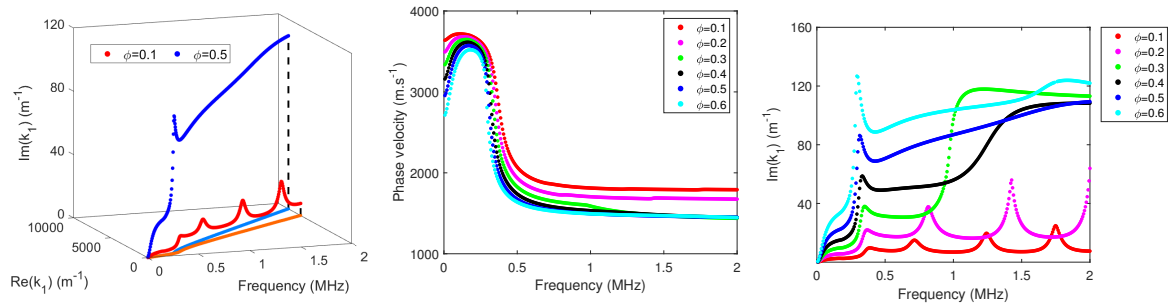

(a) (b) (c)

Figure 4: (Color online) Dependence of S_0-mode dispersion on porosity: (a) wavenumber ($\mathsf{Re}(k_1)$ and $\mathsf{Im}(k_1)$); (b) phase velocity; (c) attenuation

It worth noticing that, when considering an elastic plate at very low frequency range, the phase velocity of the S_0 mode was found to be constant (non dispersive), being approximately equal to

the compressional wave velocity. This phenomenon may be explained by the fact that, at very low frequency, as the wavelength of the compressional wave is much longer than the plate's thickness, the S_0 mode may be seen as a plane compressionnal wave propagating along axial direction of the plate. In this study where the poroelastic plates were studied, the phase velocity of S_0 mode at low frequency limit (Fig. 4) was found not be constant but very dispersive, especially when the porosity was high. In fact, it might be guessed that the dispersive feature of the S_0-branch at low frequency range lies to the dynamic behavior of of poroelastic materials. In a pororelastic medium, there exists not only one but two compressional waves, which are known as the fast and slow P-waves. While the wavelength of the fast P-wave is quasi-constant and comparable to the compressional wave in the elastic medium, the wavelength of slow P-wave is typically very small at the low-frequency limit. The presence of the slow P-wave, which is very dispersive in low-frequency, would be the reason for which the S_0 mode is dispersive at low- frequency range. We may also observe that when the porosity tends to zero, the S_0-mode branch tends to a constant function at low frequency, which is similar to elastic plate cases.

5.1.2. Validation of SAIGA-G and SAIGA-C methods

The results obtained by the proposed SAIGA-G and SAIGA-C methods were validated by comparing with the reference solution computed by conventional SAFE method. In this example, both SAIGA-G and SAIGA-C modeling are based on a single patch in which the NURBS basis functions with order q over an uniform knot vector were used. The number of elements (spans) in the patch is then given by $N_{\text{el}} = n_{\text{P}} - q = N_{\text{dof}}/n_{\text{dof}} - q$. Consequently, the total number of degrees of freedom (N_{dof}) is: $N_{\text{dof}}^{\text{SAIGA-G}} = N_{\text{dof}}^{\text{SAIGA-C}} = n_{\text{P}} \times n_{\text{dof}}$, where n_{P} is the number of control points (or nodes) and $n_{\text{dof}} = 4$ which is the number of unknowns (u_1, u_2, w_1, w_2) at each control point. On the other hand, by using the conventional SAFE method with $N_{\text{el}}^{\text{SAFE}}$ elements with q^{th}-order Lagrange interpolation function, the total number of degree of freedom is given by: $N_{\text{dof}}^{\text{SAFE}} = (q \times N_{\text{el}}^{\text{SAFE}} + 1) \times n_{\text{dof}}$.

Dispersion curves of the phase velocity and attenuation *versus* the frequency of first 14 modes in the range f = 0–2 MHz were computed by using SAIGA-G, SAIGA-C and SAFE methods. Then theses solutions were compared with the reference solution ($q = 2$, $N_{\text{dof}} = 404$) as shown in Figs. 5(a,b). In this example, all methods employed quartic-order ($q = 4$) basis functions and have the same $N_{\text{dof}} = 68$: the SAIGA-G method used 13 elements, the SAIGA-C method used 17

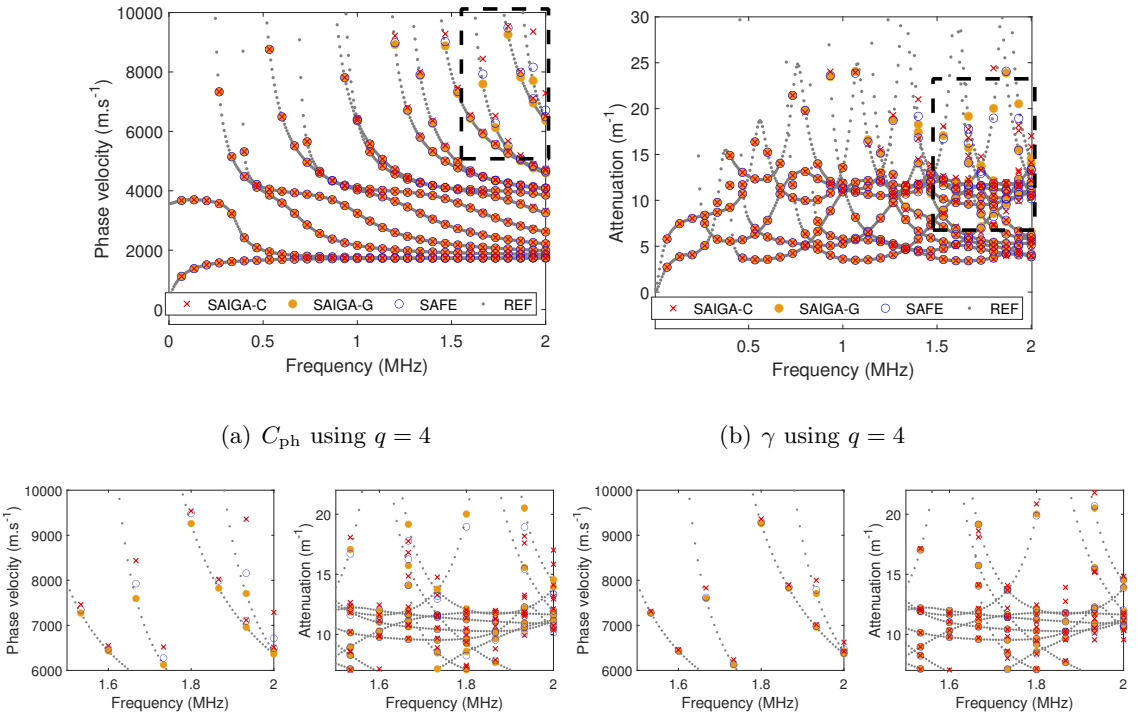

(a) C_{ph} using $q = 4$ (b) γ using $q = 4$

(c) C_{ph} with $q = 4$ (d) γ using $q = 4$ (e) C_{ph} using $q = 8$ (f) γ using $q = 8$

Figure 5: (Color online) Case of a free poroelastic layer ($\phi = 0.1$): validation of SAIGA-C, SAIGA-G and SAFE solutions computed with $q = 4$, $N_{\text{dof}} = 68$; sub-figures (c) and (d) are zoomed from the dashed-line windows in sub-figures (a) and (b), respectively.

collocation points , and the SAFE method used 4 elements. At low frequencies, all of three methods provide accurate estimations of C_{ph} as well as of γ. However, at high frequencies (1.5-2 MHz), the SAIGA-G solution has better precision than the ones obtained by SAIGA-C and SAFE methods, especially the modes presented in the dashed-line windows plotted in Fig. 5(a,b), which respectively are zoomed in Figs. 5(c,d) for a clearer comparison. Moreover, it may be observed in Figs. 5(c,d) that SAFE solutions didn't capture exactly the reference ones as the SAIGA-G solutions did, but they are better than SAIGA-C ones. In Figs. 5(e,f), we present the solutions computed by using $q = 8$ and by arranging the number of elements/spans ($N_{\text{el}}^{\text{SAIGA-C}} = N_{\text{el}}^{\text{SAIGA-G}} = 9$ and $N_{\text{el}}^{\text{SAFE}} = 2$) so that we still have $N_{\text{dof}} = 68$. It may be seen that using $q = 8$ improves the precision of SAFE solution. The precision the SAIG-C solution was even more significantly improved, although the attenuation of some modes were still not exactly predicted. This comparison affirms the fact that

the collocation based approach generally requires a higher order of NURBS basis functions than the Galerkin based approach.

Figs. 6(a,b) affirm the validation of C_{ph} solutions computed using SAIGA-G, SAIGA-C and SAFE methods for higher porosity cases ($\phi = 0.5$ and $\phi = 0.6$). Similar to the case ($\phi = 0.1$), the results of higher modes at higher frequency range (1.5-2 MHz) were shown to be less accurate. Moreover, the numerical errors seem to be more important when considering plates with higher porosity, in which the pore fluid movement becomes more significant. We may observe that the branch of mode S_0, which was continuous in the cases ($\phi = 0.1, 0.5$), turned out to be discontinuous due to excessive values of attenuation when considering a higher porosity $\phi = 0.6$. One may observe that $f \approx 0.3$ MHz corresponds to the cut-on frequency of S_1 branch at which the high valued peak was found on attenuation curve (see Fig. 4(c))

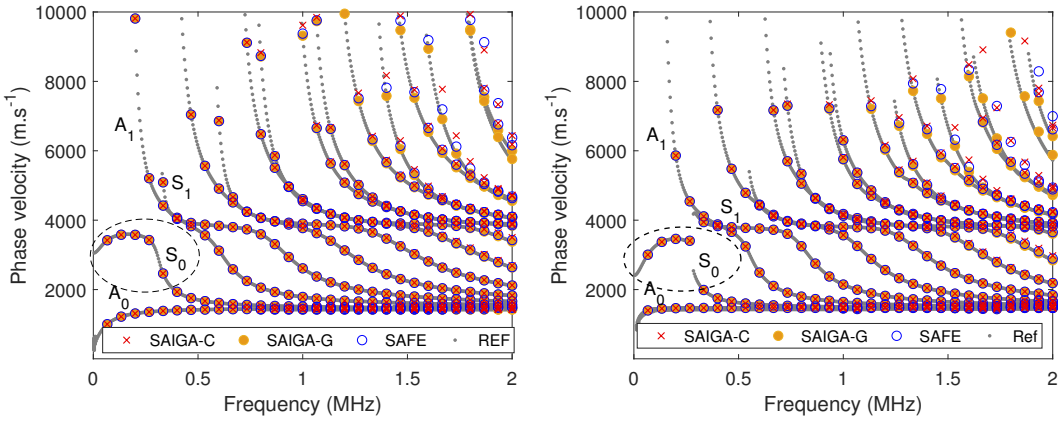

(a) $\phi = 0.5$ (b) $\phi = 0.6$

Figure 6: (Color online) Phase velocity curves of poroelastic bone layer: comparison between the SAIGA-C ($q = 4$ and $N_{\text{dof}} = 68$), SAIGA-G ($q = 4$ and $N_{\text{dof}} = 68$) and SAFE ($q = 4$ and $N_{\text{dof}} = 68$) and REF solution ($q = 2$ and $N_{\text{dof}} = 404$)

5.1.3. Convergence study

We aim to study the convergence rate of the proposed methods for evaluating the phase velocity in poroelastic plates. In particular, we are interested in investigating the accuracy of the numerical results when considering a specific mode over a frequency range. To do so, we introduce a function

$\texttt{err}(m)$ which estimates the relative errors of the numerical solution for a mode m as

$$\texttt{err}(m) = \sqrt{\frac{1}{N_f}\sum_{i=1}^{N_f}\left(\frac{C_{\text{ph}}^{num}(f_i,m) - C_{\text{ph}}^{REF}(f_i,m)}{C_{\text{ph}}^{REF}(f_i,m)}\right)^2}\,, \tag{44}$$

where N^f is the number of the frequency values used for the computation in the considered frequency range, $C_{\text{ph}}^{num}(f_i,m)$ and $C_{\text{ph}}^{REF}(f_i,m)$ denote the phase velocities of the mode m evaluated at the frequency (f_i) by using three numerical approaches, and its reference values, respectively.

The convergence analysis were performed for the mode S_0 in two cases of porosity $\phi = 0.1$ and $\phi = 0.5$. Figs. 7(a,b) depict the variation of the errors of the phase velocity of S_0-mode over the frequency range $f = 0 - 2$ MHz *versus* the number of DOF. Different orders q of NURBS and Lagrange basis functions were investigated. Overall, the error analysis presented in Figs. 7(a,b) shows that all methods (SAFE, SAIGA-C, SAIGA-G) implied the h- and p-convergences as expected.

While using the SAFE method with $q = 4$, we found that the numerical errors (in the both cases $\phi = 0.1$ and $\phi = 0.5$) are not efficiently reduced by applying mesh refinement. Using higher-orders $(q = 6, 8, 10)$ allows to improve significantly the accuracy solutions. Moreover, the convergence rate (*i.e* the slope of the error curves) are shown to be increases when using higher-order Lagrangian shape function. A similar comment would be made regarding the errors of SAIGA-C solutions. It would also notice that the numerical errors of SAFE are slightly different than the one of SAIGA-C and this difference seems to be more significant when the porosity is higher ($\phi = 0.5$). However, the convergence rate of SAIGA-C, which is slower than of SAFE when using *low-order* basis functions $(q = 4, 6)$, may be faster than when using *high-order* basis functions $(q = 8, 10)$.

For both cases $\phi = 0.1$ and $\phi = 0.5$, it may be found that the SAIGA-G errors using a q-order NURBS basis function is much smaller comparing with to the errors obtained from SAIGA-C or SAFE methods which used the same order basis function. For example, to achieve a solution having numerical error about 10^{-3}, while using $q = 6$ SAIGA-C and SAFE require solving a system of about N_{dof}=100, using $q = 6$ SAIGA-G only requires a system with only N_{dof}=56. Overall, the convergence rates *versus* N_{dof} using SAIGA-G method were shown to be much faster than using SAIGA-C or SAFE methods. Moreover, the numerical errors weren't significantly reduced by increasing q from 8 to 10. Hence, using $p = 8$ would be a reasonable choice for this problem in practice.

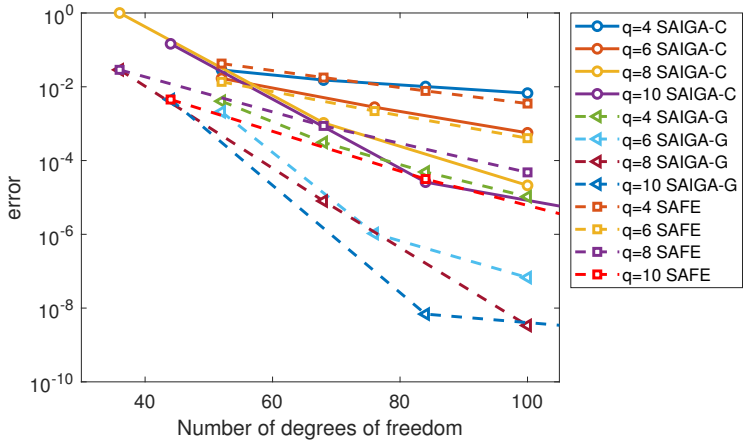

(a) ϕ=0.1

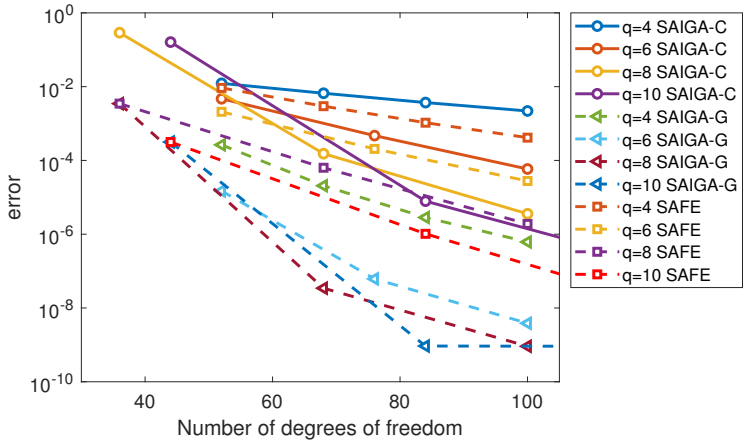

(b) ϕ=0.5

Figure 7: (Color online) Error convergence of S_0-mode computed for $\phi = 0.1$ and $\phi = 0.5$ by using SAFE, SAIGA-C and SAIGA-G methods

5.2. Case of a poroelastic plate immersed in fluids

Let us consider the case of a poroelastic bone plate, which has been studied in the previous section, but now is coupled with two half-spaces of water loaded on both sides as shown in Fig. 1. The acoustic properties of water are given by $\rho_1 = \rho_2 = 1000$ kg.m^{-3} and $c_1 = c_2 = 1500$ m.s^{-1}. The infinite fluid domains Ω_1^f and Ω_2^f are modeled as finite-thickness layers with $h_1^f = h_2^f = 4$ mm. To avoid the non-physical reflection from the upper and lower boundaries, we introduce 2 mm-thickness PMLs at the top $\bar{\Omega}_1^f$ and at the down of $\bar{\Omega}_2^f$, respectively. It worth noticing that the PMLs

have been shown to be efficient for the SAFE-based simulation of leaky guided waves in several previous works [55, 18]. In this study, the range of frequencies of interest is from 0 to 2 MHz, then PML parameters h^{pml} (PML thickness) and $\gamma_2(x_2)$ (PML function) (see Eq. A.3) were chosen by: $\hat{\gamma}_2 = 3 + 12\text{i}$ and $h^{\text{pml}} = 2.5$ mm. In addition, free pressure boundary conditions ($p_j = 0$) were imposed at the exterior boundaries of two fluid domains.

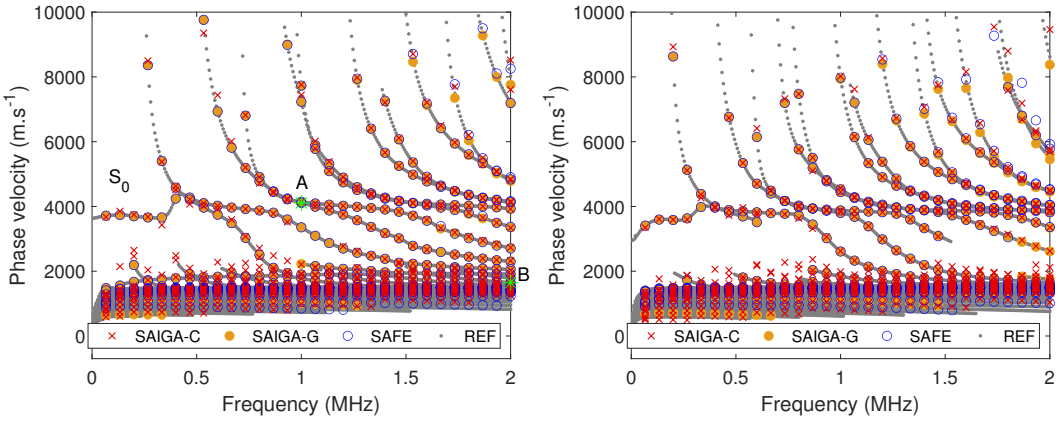

(a) $\phi = 0.1$ (b) $\phi = 0.5$

Figure 8: (Color online) Dispersion curves of immersed poroelastic bone layer: comparison between the SAIGA-C ($q = 4$ and $N_{\text{dof}} = 118$), SAIGA-G ($q = 4$ and $N_{\text{dof}} = 118$) and SAFE ($q = 4$ and $N_{\text{dof}} = 118$) and REF solution ($q = 2$ and $N_{\text{dof}} = 566$).

Fig. 8 aims to compare the dispersion curves of leaky guided waves obtained using SAIGA-G, SAIGA-C and the conventional SAFE method with respect to the reference solution (REF) obtained by using SAFE with a very fine mesh. All of three solutions were computed by using $q = 4$ (NURBS or Lagrange functions), and all associated systems have $N_{\text{dof}} = 118$, in which the numbers of DOF in the poroelastic layer and each fluid layer are $N^s_{\text{dof}} = 68$ and $N^{hs}_{\text{dof}} = 25$, respectively. Two cases of porosity ($\phi = 0.1$ and $\phi = 0.5$) were considered as shown in Fig. 8(a) and Fig. 8(b), respectively. For both porosities, the SAIGA-G solutions were shown to have better agreement with the REF solutions. In the case $\phi = 0.1$, the numerical evaluation of C_{ph} using SAIGA-C or SAFE were failed for some modes (*e.g* on the S_0 branches). Note that similar issues were also reported in Hayashi *et al* [55] when studying an elastic plate immersed in fluids. Interestingly, it was found that using SAIGA-G method (with the same shape function order $q = 4$),

allows to capture perfectly all the points along the dispersion curve. These results exhibits the effectiveness of using NUBRS-based shape functions in this context. In the case $\phi = 0.1$, SAIGA-C and SAFE have a significant errors at the higher modes and frequencies whereas SAIGA-G is in very good agreement with the REF solution. The good approximation of SAIGA-G bring to a better presentation of discontinuous modes.

The attenuation of the S_0 mode is presented in Fig 9 for the porosity of $\phi = 0.1$ and $\phi = 0.5$. In the case $\phi = 0.1$, it may be seen that the presence of exterior fluids completely changes the attenuation of the considered mode. In this case, as the porosity is small, the attenuation caused by Darcy's infiltration effect in the considered porelastic material is weak. Hence the main contribution to the attenuation to the S_0 mode is due to the leaky phenomena, in which the some energies of guided-waves are leaked into the surrounded fluid domains. When the porosity is more important ($\phi = 0.5$), the Darcy's infiltration effect in the porous material becomes much more important. Consequently, the contribution of leaky effect to the attenuation of guided waves is not dominant, even it is shown to be very significant, especially at high frequency range.

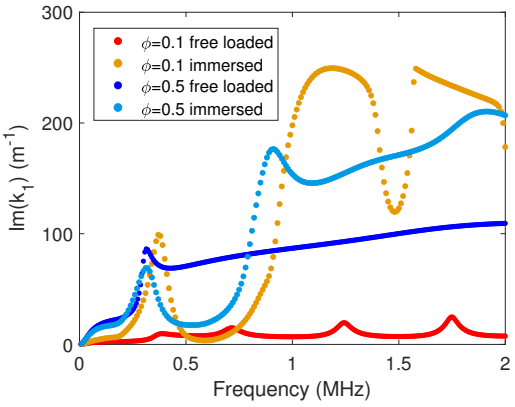

Figure 9: (Color online) Attenuation curves of S_0 mode for $\phi = 0.1$ and $\phi = 0.5$ for free loaded and immersed poroelastic plate

In order to examine the continuity in the shape modes, we first consider a mode in the dispersion curve (marked as point A in Fig. 8) which has C_{ph}=4047 m.s^{-1} at f=1 MHz. Figures 10(a,b) present the shape modes of the displacement and pressure fields of this mode computed by three proposed methods. Note that the displacements in the fluid domains were derived from the gradient of pressure field (see Eq. 2). In the poroelastic layer, the stresses and pressure were derived the

solutions of $\mathbf{U}$ and $\mathbf{W}$ by using Eqs. (3) and (9), respectively. At the fluid-solid interface, the expected conditions of continuity of u_2 and p was perfectly verified for the SAIGA-G's solutions. However, some small discontinuities were found when using SAFE or SAIGA-C methods. As it could be expected, the SAIGA and SAFE solutions of displacement (u_2) and pressure (p_j) fields are progressively attenuated in the PML domains. It has also been checked that the obtained numerical solutions are not influenced by the distance between the PML and the poroelastic-fluid interface (data not shown). Thus, the use of PMLs as shown in Appendix A is an efficient way to consider the halfspace fluid domains in the considered study.

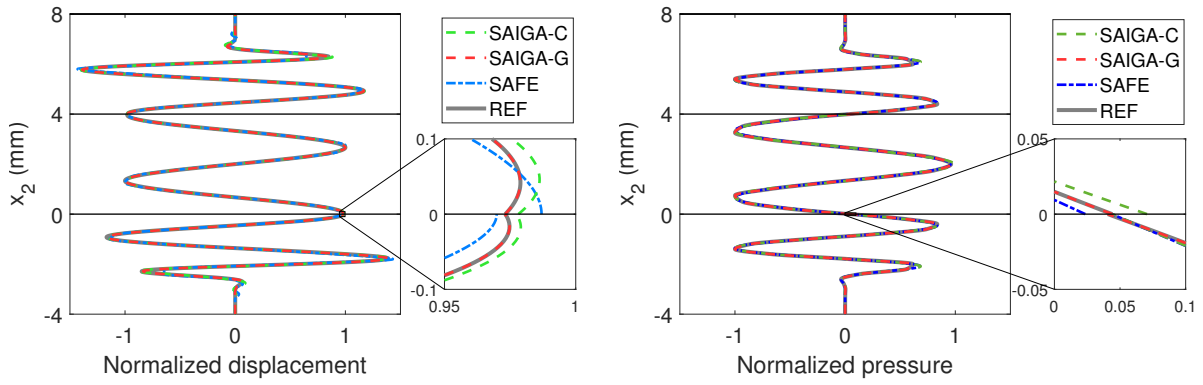

(a) displacement u_2^f, u_2, u_2^f (b) pressure p_1, p, p_2

Figure 10: (Color online) Continuity of the mode shapes at f=1 MHz , C_{ph}=4047 m.s^{-1} (point A in Fig. 8(a)) of immersed poroelastic cortical bone plate $\phi = 0.1$: comparison between the SAIGA-C ($q = 4$ and $N_{\text{dof}} = 118$), SAIGA-G ($q = 4$ and $N_{\text{dof}} = 118$),SAFE ($q = 4$ and $N_{\text{dof}} = 118$) and REF solution ($q = 2$ and $N_{\text{dof}} = 566$).

We next consider a mode at high frequency ($f = 2$ MHz) which corresponds to the point B in Fig. 8(a)). Figs 11(a,b) depicts images of the displacement and pressure fields of this mode in the $(\mathbf{e}_1, \mathbf{e}_2)$ plane. The comparison of mode shapes computed by using SAFE, SAIGA-C and SAIGA-G methods are presented in Figs. 12(a,b,c,d). For this mode , using SAGA-G method ($q = 4$ and $N_{\text{dof}} = 118$) may produce perfectly the reference solutions of u_2, w_2, p and σ_{22}, which are expected to be continuous over all domains, even at the interfaces. However, at this high frequency, the considered mode shapes computed by SAFE and SAIGA-C methods, which were based on the same q and N_{dof}, may be found to be very erroneous, not only at the solid-fluid interfaces, but also over all domains. Hence, using the SAIGA-G method would be more appropriate for computing

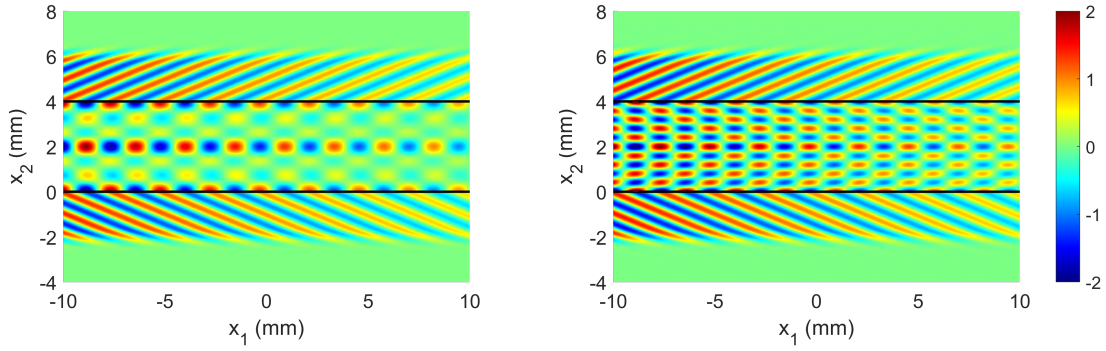

(a) displacement $u_2^{f_1}$, u_2, $u_2^{f_2}$ (b) pressure p_1, p^f, p_2

Figure 11: (Color online) Leaky wave propagation in an immersed poroelastic plate $\phi = 0.1$: symmetric mode shapes at f=2 MHz , C_{ph}=2218 m.s^{-1} (point B in Fig. 8(a)) (a) displacement and (b) pressure fields

the mode shapes when higher frequency needs to considered.

6. Conclusion

This presented works attempted to enlighten the potential of two SAIGA-based methods for studying the guided-waves in two-dimensional poroelastic plates with or without surrounding fluids. Two semi-analytical approaches, based on isogeometric Galerkin or collocation analysis (denoted by SAIGA-G and SAIGA-C, respectively) were developed. Due to the presence of the interstitial fluid phase, guided waves in the poroelastic plates are strongly attenuated, especially when considering the cases of higher porosity and/or at high frequency. From computational point of view, determination of guided waves' characteristics in poroelastic plates lead to quadratic eigenvalue problems of which all eigenvalues are complex. By comparing with the conventional SAFE method in which Lagrangian interpolation functions are used, the present study showed that using NURBS-based interpolation function may yield much more precise numerical solutions of complex-valued wavenumbers as well mode shapes of the guied-wave modes. Moreover, the PML technique may be introduced without difficulties for efficiently simulating the infinite surrounding fluid domains in proposed formulations. It was shown that using SAIGA-C method doesn't give significant advantages in terms of accuracy in comparison with the conventional SAFE method. However, the implementation of SAIGA-C method, which is based on the disretization of strong form equations, is straightforward and easier than the ones of SAFE or SAIGA-G methods, which are based on

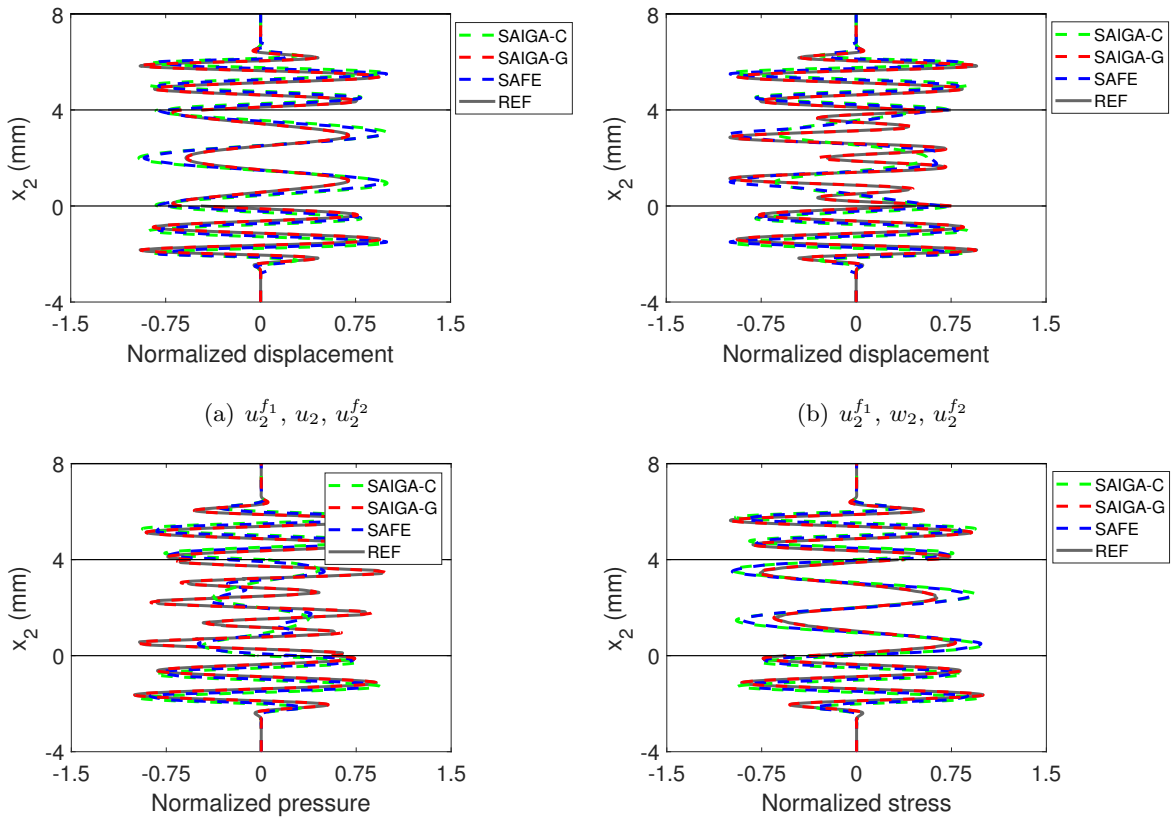

(a) $u_2^{f_1}$, u_2, $u_2^{f_2}$

(b) $u_2^{f_1}$, w_2, $u_2^{f_2}$

(c) p_1, p, p_2

(d) p_1, σ_{22}, p_2

Figure 12: (Color online) Mode shapes at f=2 MHz , C_{ph}=2218 m.s^{-1} (point B in Fig. 8(a)) for an immersed poroelastic cortical bone plate $\phi = 0.1$: comparison between the SAFE ($q = 4$ and $N_{\text{dof}} = 118$), SAIGA ($q = 4$ and $N_{\text{dof}} = 118$) and REF solution ($q = 2$ and $N_{\text{dof}} = 566$).

the discretization of weak form equations [56]. It worth noticing that, by considering the 2D problems, the advantages of isogeometric methods were achieved thank to the high continuity feature of NURBS functions. For 3D problems, the SAIGA methods would be expected to be even more efficient, because they allow to describe more precisely complex geometries [38].

Appendix A. Perfectly Matched Layer (PML)

Finite element modeling of open waveguides requires special techniques to take into account the radiation condition of infinite surrounding media. In [57], a so-called 2.5D FEM-BEM method in which the SAFE method coupled with the boundary element method (BEM) has been proposed to simulate open waveguides. This method leads to a nonlinear eigenvalue problem that requires

expensive computational effort. Another technique represents the infinite medium by an absorbing layer (AL) [22, 58]. In this layer, a physical viscosity, which artificially increases with the distance from the central axis for the waveguide's core, is introduced. In practice, sufficient large layers is required in order to avoid artificial reflections by the absorbing layer, leading to a large set of eigenvalue equations and increases the computational cost. Recently, the Perfectly Matched Layer (PML) is proposed to model the infinite surrounding medium (solid or fluid) in the context of SAFE [18, 59, 60].

From mathematical point of view, the PML can be considered as a result of a mapping into complex coordinate, where the solutions of wave equations decay exponentially (as the new coordinate is complex)[61]. Therefore, the infinite medium can be truncated into a finite domain. The new stretched coordinates $\tilde{x}_1(x_1)$ and $\tilde{x}_2(x_2)$ in the waveguide are defined as

$$\tilde{x}_1(x_1) = x_1, \quad \tilde{x}_2(x_2) = \int_0^{x_2} \gamma_2(x_2) dx_2, \tag{A.1}$$

where $\gamma_2(x_2)$ are non-zero, continuous, complex-valued coordinate stretching functions, also called PML functions, which satisfy:

$$\gamma_2(x_2) = 1 \text{ for } |x_2| \leq d_{x_2} \text{ and } \mathrm{Im}\{\gamma_2(x_2)\} > 0 \text{ for } |x_2| > d_{x_2} \tag{A.2}$$

where (d_{x_2}) is the position of the interfaces. We denote by h^{pml} the PML thicknesses in the e_2 directions. On the exterior boundary of the PML, the boundary condition can be arbitrarily chosen (Dirichlet or Neumann type). The absorption efficiency of leaky waves in the PML strongly depends on the choice of the PML function (γ_2), the position of the interface (d_{x_2}) and the thickness (h^{pml}). There are a number of variants to choose for the γ_2 function. For this study, a continuous parabolic function for both the real and imaginary parts of the PML function is therefore used which has demonstrated good performance in problems in the frequency domain [59, 62]:

$$\gamma_2(x_2) = \begin{cases} 1 & \text{if } |x_2| \leq d_{x_2}. \\ 1 + \hat{\gamma}_2 \left(\frac{|x_2| - d_{x_2}}{h^{pml}} \right)^2 & \text{if } |x_2| > d_{x_2}. \end{cases} \tag{A.3}$$

Appendix B. Determination of poroelastic parameters

To describe the behavior of the poroelastic bone plate, the drained elasticity tensor $\mathbb{C}$ as well as Biot's effective coefficients $\boldsymbol{\alpha}$ and $\boldsymbol{M}$ used in (3) and (4) should be provided. For this study,

these parameters are derived from the characteristics of the interstitial fluid and solid skeleton phases by using a continuum micro-mechanics model proposed by Hellmich et al. [63]. According to this model, the micro-pores at the micro-structural scale are regarded as cylindrical pores with a circular cross section. In drained condition, the constitutive behavior of the material inside the pores does not possess stiffness. Hence, the estimated drained micro-structural stiffness of the bone whose solid bone matrix's elasticity tensor is $\mathbb{C}^m$ reads:

$$\mathbb{C} = (1-\phi)\mathbb{C}^m : \left\{ (1-\phi)\mathbb{I} + \phi\left[\mathbb{I} - \mathbb{P}^{cyl} : \mathbb{C}^m\right]^{-1} \right\}^{-1} , \tag{B.1}$$

where $\mathbb{I}$ denotes the fourth-order identity tensor; $\mathbb{P}^{cyl}$ the fourth-order tensor is the Hill's tensor for materials with periodical cylindrical inclusions, which may be derived in closed form [63]. The tensor $\boldsymbol{\alpha}$ the constant M can be then evaluated by [46, 48]:

$$\boldsymbol{\alpha} = \mathbf{I} - \mathbb{C} : (\mathbb{S}^m : \mathbf{I}), \qquad -\frac{1}{M} = C - \boldsymbol{\alpha} : \mathbb{S} : \boldsymbol{\alpha} , \tag{B.2}$$

where $\mathbb{S} = (\mathbb{C})^{-1}$ and $\mathbb{S}_m = (\mathbb{C}_m)^{-1}$ are respectively the drained and solid material compliance tensors, I designates the second-order tensor identity and the scalar C denotes the effective compressibility of porous matrix material, which is given by

$$C = \frac{1}{K} - \frac{1}{K_m} + \phi\left(\frac{1}{K_f} - \frac{1}{K_m}\right) , \tag{B.3}$$

where $K = (\mathbf{I} : \mathbb{S} : \mathbf{I})^{-1}$, K_f and $K_m = (\mathbf{I} : \mathbb{S}_m : \mathbf{I})^{-1}$ are the bulk moduli of the drained porous matrix and of the interstitial fluid and of the poroelastic material, respectively.

References

[1] N. Gorbushin, S. Naili, V.-H. Nguyen, Optimizing microstructure of a poroelastic layer with cylindrical pores for absorption properties, Mechanics Research Communications 102 (2019) 103422.

[2] E. Ogam, Z. E. A. Fellah, G. Ogam, N. O. Ongwen, A. O. Oduor, Investigation of long acoustic waveguides for the very low frequency characterization of monolayer and stratified air-saturated poroelastic materials, Applied Acoustics 182 (2021) 108200.

[3] S.-Y. Zhang, D.-J. Yan, Y.-S. Wang, Y.-F. Wang, V. Laude, Wave propagation in one-dimensional fluid-saturated porous phononic crystals with partial-open pore interfaces, International Journal of Mechanical Sciences 195 (2021) 106227.

[4] D. Chimenti, Review of air-coupled ultrasonic materials characterization, Ultrasonics 54 (7) (2014) 1804–1816.

[5] M. Thelen, N. Bochud, M. Brinker, C. Prada, P. Huber, Laser-excited elastic guided waves reveal the complex mechanics of nanoporous silicon, arXiv preprint arXiv:2010.14947 (2020).

[6] V.-H. Nguyen, S. Naili, Semi-analytical solution of transient plane waves transmitted through a transversely isotropic poroelastic plate immersed in fluid, Journal of Engineering Mathematics 86 (1) (2014) 125–138.

[7] M. A. Biot, Theory of propagation of elastic waves in a fluid-saturated porous solid. ii. higher frequency range, The Journal of the Acoustical Society of America 28 (2) (1956) 179–191.

[8] C. Zimmerman, M. Stern, Analytical solutions for harmonic wave propagation in poroelastic media, Journal of engineering mechanics 120 (10) (1994) 2154–2178.

[9] T. Senjuntichai, R. Rajapakse, Dynamic Green's functions of homogeneous poroelastic half-plane, Journal of Engineering Mechanics 120 (11) (1994) 2381–2404.

[10] G. Belloncle, H. Franklin, F. Luppé, J. Conoir, Normal modes of a poroelastic plate and their relation to the reflection and transmission coefficients, Ultrasonics 41 (3) (2003) 207–216.

[11] H. Franklin, S. Derible, C. Popa, Expansions of reflected-transmitted signals to estimate the slow wave strength in fluid-saturated porous layers, The Journal of the Acoustical Society of America 128 (3) (2010) 1073.

[12] G. Degrande, G. De Roeck, P. Van den Broeck, D. Smeulders, Wave propagation in layered dry, saturated and unsaturated poroelastic media, International Journal of Solids and Structures 35 (34-35) (1998) 4753–4778.

[13] A. Mesgouez, G. Lefeuve-Mesgouez, Transient solution for multilayered poroviscoelastic media obtained by an exact stiffness matrix formulation, International journal for numerical and analytical methods in geomechanics 33 (18) (2009) 1911–1931.

[14] C. Baron, S. Naili, Propagation of elastic waves in a fluid-loaded anisotropic functionally graded waveguide: Application to ultrasound characterization, The Journal of the Acoustical Society of America 127 (3) (2010) 1307–1317.

[15] A. Geslain, J.-P. Groby, O. Dazel, S. Mahasaranon, K. Horoshenkov, A. Khan, An application of the peano series expansion to predict sound propagation in materials with continuous pore stratification, The Journal of the Acoustical Society of America 132 (1) (2012) 208–215.

[16] O. Dazel, J.-P. Groby, B. Brouard, C. Potel, A stable method to model the acoustic response of multilayered structures, Journal of Applied Physics 113 (8) (2013) 083506.

[17] J. Jocker, D. Smeulders, G. Drijkoningen, C. van der Lee, A. Kalfsbeek, Matrix propagator method for layered porous media: Analytical expressions and stability criteria, Geophysics 69 (4) (2004) 1071–1081.

[18] P. Zuo, Z. Fan, SAFE-PML approach for modal study of waveguides with arbitrary cross sections immersed in inviscid fluid, Journal of Sound and Vibration 406 (2017) 181–196.

[19] V.-H. Nguyen, T. N. Tran, M. D. Sacchi, S. Naili, L. H. Le, Computing dispersion curves of elastic/viscoelastic transversely-isotropic bone plates coupled with soft tissue and marrow using semi-analytical finite element (SAFE) method, Computers in Biology and Medicine 87 (2017) 371–381.

[20] C. Li, Q. Han, Z. Wang, X. Wu, Analysis of wave propagation in functionally graded piezoelectric composite plates reinforced with graphene platelets, Applied Mathematical Modelling 81 (2020) 487–505.

[21] C. Li, Q. Han, Semi-analytical wave characteristics analysis of graphene-reinforced piezoelectric polymer nanocomposite cylindrical shells, International Journal of Mechanical Sciences 186 (2020) 105890.

[22] Z. Fan, M. Lowe, M. Castaings, C. Bacon, Torsional waves propagation along a waveguide of arbitrary cross section immersed in a perfect fluid, The Journal of the Acoustical Society of America 124 (4) (2008) 2002–2010.

[23] D. Pereira, G. Haiat, J. Fernandes, P. Belanger, Simulation of acoustic guided wave propagation in cortical bone using a semi-analytical finite element method, The Journal of the Acoustical Society of America 141 (4) (2017) 2538–2547.

[24] V.-H. Nguyen, S. Naili, Ultrasonic wave propagation in viscoelastic cortical bone plate coupled with fluids: a spectral finite element study, Computer Methods in Biomechanics and Biomedical Engineering 16 (9) (2013) 963–974.

[25] V.-H. Nguyen, S. Naili, Simulation of ultrasonic wave propagation in anisotropic poroelastic bone plate using hybrid spectral/finite element method, International Journal for Numerical Methods in Biomedical Engineering 28 (8) (2012) 861–876.

[26] R. Xia, J. Zhu, J. Yi, S. Shao, Z. Li, Guided wave propagation in multilayered periodic piezoelectric plate with a mirror plane, International Journal of Mechanical Sciences 204 (2021) 106539.

[27] Z. Yang, K. Liu, K. Zhou, Y. Liang, J. Zhang, Y. Zheng, D. Gao, S. Ma, Z. Wu, Investigation of thermo-acoustoelastic guided waves by semi-analytical finite element method, Ultrasonics 106 (2020) 106141.

[28] P. J. Matuszyk, L. F. Demkowicz, Solution of coupled poroelastic/acoustic/elastic wave propagation problems using automatic hp-adaptivity, Computer Methods in Applied Mechanics and Engineering 281 (2014) 54–80.

[29] C. Morency, J. Tromp, Spectral-element simulations of wave propagation in porous media, Geophysical Journal International 175 (1) (2008) 301–345.

[30] N.-E. Hörlin, 3d hierarchical hp-FEM applied to elasto-acoustic modelling of layered porous media, Journal of Sound and Vibration 285 (1-2) (2005) 341–363.

[31] F. Treyssede, Spectral element computation of high-frequency leaky modes in three-dimensional solid waveguides, Journal of Computational Physics 314 (2016) 341–354.

[32] M. K. Kalkowski, J. M. Muggleton, E. Rustighi, Axisymmetric semi-analytical finite elements for modelling waves in buried/submerged fluid-filled waveguides, Computers & Structures 196 (2018) 327–340.

[33] F. Seyfaddini, H. Nguyen-Xuan, V.-H. Nguyen, A semi-analytical isogeometric analysis for wave dispersion in functionally graded plates immersed in fluids, Acta Mechanica 232 (2021) 15–32.

[34] T. J. Hughes, J. A. Evans, A. Reali, Finite element and NURBS approximations of eigenvalue, boundary-value, and initial-value problems, Computer Methods in Applied Mechanics and Engineering 272 (2014) 290 – 320.

[35] J. Cottrell, A. Reali, Y. Bazilevs, T. Hughes, Isogeometric analysis of structural vibrations, Computer Methods in Applied Mechanics and Engineering 195 (41) (2006) 5257 – 5296.

[36] C. Willberg, S. Duczek, J. V. Perez, D. Schmicker, U. Gabbert, Comparison of different higher order finite element schemes for the simulation of Lamb waves, Computer Methods in Applied Mechanics and Engineering 241 (2012) 246–261.

[37] H. Gravenkamp, S. Natarajan, W. Dornisch, On the use of NURBS-based discretizations in the scaled boundary finite element method for wave propagation problems, Computer Methods in Applied Mechanics and Engineering 315 (2017) 867–880.

[38] F. Seyfaddini, H. Nguyen-Xuan, V.-H. Nguyen, Wave dispersion analysis of three-dimensional vibroacoustic waveguides with semi-analytical isogeometric method, Computer Methods in Applied Mechanics and Engineering 385 (2021) 114043.

[39] C. Li, Q. Han, Guided waves propagation in sandwich cylindrical structures with functionally graded graphene-epoxy core and piezoelectric surface layers, Journal of Sandwich Structures & Materials (2020).

[40] F. Irzal, J. J. Remmers, C. V. Verhoosel, R. de Borst, Isogeometric finite element analysis of poroelasticity, International Journal for Numerical and Analytical Methods in Geomechanics 37 (12) (2013) 1891–1907.

[41] S. Morganti, C. Callari, F. Auricchio, A. Reali, Mixed isogeometric collocation methods for the simulation of poromechanics problems in 1D, Meccanica 53 (6) (2018) 1441–1454.

[42] F. Auricchio, L. B. Da Veiga, T. J. Hughes, A. Reali, G. Sangalli, Isogeometric collocation for elastostatics and explicit dynamics, Computer Methods in Applied Mechanics and Engineering 249 (2012) 2–14.

[43] M. A. Biot, Theory of elasticity and consolidation for a porous anisotropic solid, Journal of Applied physics 26 (2) (1955) 182–185.

[44] M. A. Biot, D. Willis, The elastic coefficients of the theory of consolidation, J. Appl. Mech 24 (1957) 594–601.

[45] O. Coussy, Poromechanics, John Wiley & Sons, 2004.

[46] A.-D. Cheng, Material coefficients of anisotropic poroelasticity, International Journal of Rock Mechanics and Mining Sciences 34 (2) (1997) 199–205.

[47] S. C. Cowin, A recasting of anisotropic poroelasticity in matrices of tensor components, Transport in Porous Media 50 (1-2) (2003) 35–56.

[48] M. Thompson, J. Willis, A reformation of the equations of anisotropic poroelasticity, Journal of Applied Mechanics 58 (3) (1991) 612–616.

[49] J. M. Carcione, C. Morency, J. E. Santos, Computational poroelasticity — a review, GEOPHYSICS 75 (5) (2010) 75A229–75A243.

[50] J. M. Carcione, Wave fields in real media: Wave propagation in anisotropic, anelastic, porous and electromagnetic media, Vol. 38, Elsevier, 2007.

[51] D. L. Johnson, J. Koplik, R. Dashen, Theory of dynamic permeability and tortuosity in fluid-saturated porous media, Journal of Fluid Mechanics 176 (1987) 379–402.

[52] L. Dedè, C. Jaggli, A. Quarteroni, Isogeometric numerical dispersion analysis for two-dimensional elastic wave propagation, Computer Methods in Applied Mechanics and Engineering 284 (2015) 320 – 348.

[53] J. O. Parra, P.-c. Xu, Dispersion and attenuation of acoustic guided waves in layered fluid-filled porous media, The Journal of the Acoustical Society of America 95 (1) (1994) 91–98.

[54] P. C. Vinh, A. Aoudia, P. T. H. Giang, Rayleigh waves in orthotropic fluid-saturated porous media, Wave Motion 61 (2016) 73–82.

[55] T. Hayashi, D. Inoue, Calculation of leaky Lamb waves with a semi-analytical finite element method, Ultrasonics 54 (6) (2014) 1460 – 1469.

[56] A. Reali, T. J. R. Hughes, An Introduction to Isogeometric Collocation Methods, Springer Vienna, Vienna, 2015, pp. 173–204.

[57] M. Mazzotti, I. Bartoli, A. Marzani, E. Viola, A coupled SAFE-2.5D BEM approach for the dispersion analysis of damped leaky guided waves in embedded waveguides of arbitrary cross-section, Ultrasonics 53 (7) (2013) 1227–1241.

[58] M. Castaings, M. Lowe, Finite element model for waves guided along solid systems of arbitrary section coupled

to infinite solid media, The Journal of the Acoustical Society of America 123 (2) (2008) 696–708.

[59] K.-L. Nguyen, F. Treyssede, C. Hazard, Numerical modeling of three-dimensional open elastic waveguides combining semi-analytical finite element and perfectly matched layer methods, Journal of Sound and Vibration 344 (2015) 158–178.

[60] S. Kim, J. Pasciak, The computation of resonances in open systems using a perfectly matched layer, Mathematics of Computation 78 (267) (2009) 1375–1398.

[61] F. Teixeira, W. C. Chew, Complex space approach to perfectly matched layers: a review and some new developments, International Journal of Numerical Modelling: Electronic Networks, Devices and Fields 13 (5) (2000) 441–455.

[62] P. Zuo, X. Yu, Z. Fan, Numerical modeling of embedded solid waveguides using SAFE-PML approach using a commercially available finite element package, NDT & E International 90 (2017) 11–23.

[63] C. Hellmich, F.-J. Ulm, Microporodynamics of bones: prediction of the Frenkel–Biot slow compressional wave, Journal of Engineering Mechanics 131 (9) (2005) 918–927.

Poroelastic plate immersed in fluids

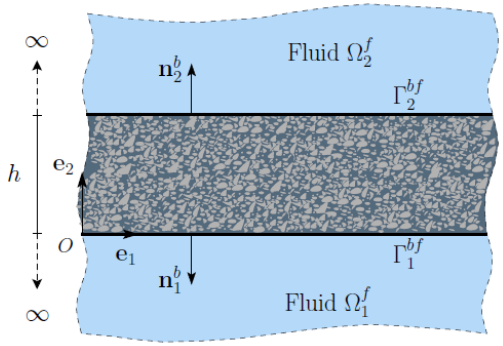

Guided-wave analysis
using
semi-analytical isogeometric methods

- *Galerkin method (SAGA-G)*
- *Collocation method (SAIGA-C)*

Dispersion curves

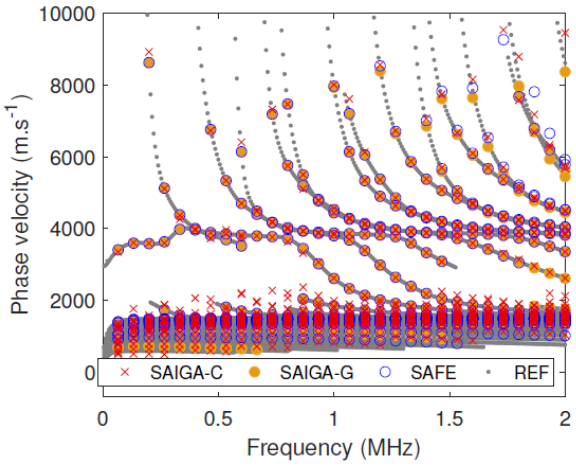

Fast convergence of phase velocity

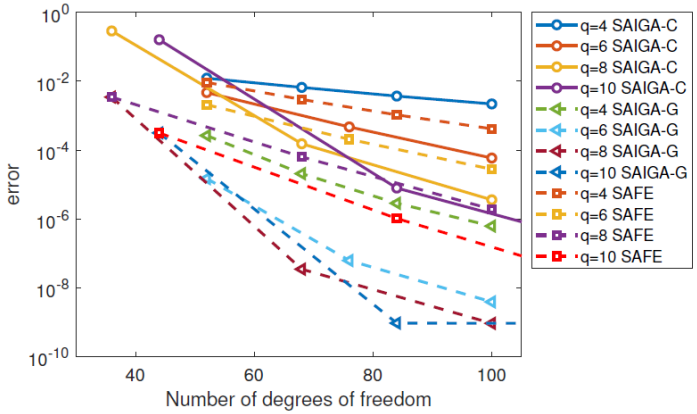

High continuity of mode shapes